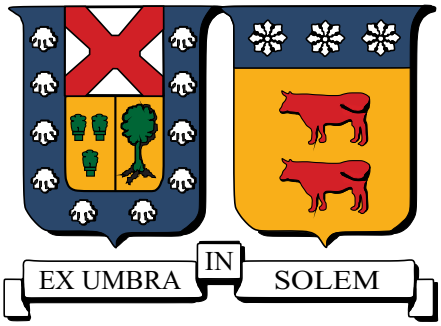

UNIVERSIDAD TÉCNICA FEDERICO SANTA MARÍA
DEPARTAMENTO DE OBRAS CIVILES

INVERSIÓN DE BATIMETRÍA EN LA ZONA DE ROMPIENTES VÍA ASIMILACIÓN DE MEDICIONES REMOTAS DE DISIPACIÓN DE ENERGÍA POR ROTURA DEL OLEAJE

FRANCISCO JOSÉ SOTO SIMPSON

Ingeniero Civil
Magíster en Ciencias de la Ingeniería Civil

Agosto de 2020

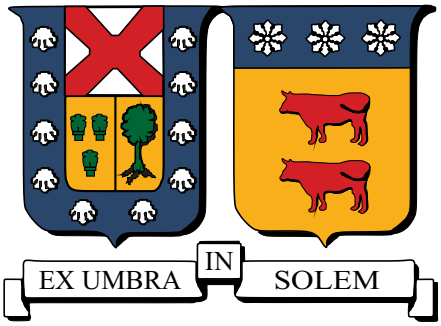

UNIVERSIDAD TÉCNICA FEDERICO SANTA MARÍA
DEPARTAMENTO DE OBRAS CIVILES

INVERSIÓN DE BATIMETRÍA EN LA ZONA DE ROMPIENTES VÍA ASIMILACIÓN DE MEDICIONES REMOTAS DE DISIPACIÓN DE ENERGÍA POR ROTURA DEL OLEAJE

Tesis de Grado y Memoria de Título presentada por
FRANCISCO JOSÉ SOTO SIMPSON

como requisito parcial para optar al título de
Ingeniero Civil

y al grado de
Magíster en Ciencias de la Ingeniería Civil

Profesor Guía
Dr. Patricio Andrés Catalán Mondaca

Agosto de 2020

TÍTULO DE LA TESIS

INVERSIÓN DE BATIMETRÍA EN LA ZONA DE ROMPIENTES VÍA ASIMILACIÓN DE MEDICIONES REMOTAS DE DISIPACIÓN DE ENERGÍA POR ROTURA DEL OLEAJE

AUTOR

FRANCISCO JOSÉ SOTO SIMPSON

TRABAJO DE TESIS, presentado en cumplimiento parcial de los requisitos para el título de **Ingeniero Civil** y el grado de **Magíster en Ciencias de la Ingeniería Civil** de la Universidad Técnica Federico Santa María.

Dr. Patricio Catalán Mondaca _____

_____

_____

Valparaíso, Chile, Agosto de 2020.

"Resistir es tan cobarde o tan
heroico como renunciar."

Manuel Rojas

"Tengo tiempo
Para saber si lo que sueño
Concluye en algo
No te apures ya más, loco
Porque es entonces cuando las horas
Bajan..."

Luis Alberto Spinetta

Resumen

La batimetría es un factor determinante para predecir la transformación del oleaje y corrientes en la zona costera, sin embargo, es usualmente desconocida y difícil de medir.

Afortunadamente, como la influencia del fondo en la mayoría de los procesos hidrodinámicos costeros es bien comprendida, es posible plantear un problema inverso, i.e., inversión de batimetría, en el que ocupando observaciones y la física que reproducen los modelos se puede recuperar la topografía subacuática. En las últimas décadas, gracias a la proliferación de cámaras digitales y otros sensores remotos, se han explotado dos dependencias de la profundidad: la celeridad de las olas y la disipación por rotura (*Holman and Haller* (2013)).

En la primera (e.g. *Holman et al.* (2013)), se ocupan técnicas de procesamiento de señales para estimar la velocidad de propagación del oleaje y luego la ecuación de dispersión lineal para estimar la profundidad. Sus resultados son satisfactorios fuera de la zona de rompientes pero su precisión decae hacia la orilla, debido a no linealidades del oleaje en aguas someras (*Catalán and Haller* (2008)) y a la aceleración aparente que miden los instrumentos en el proceso de rotura (*Brodie et al.* (2018)). Otros (e.g. *Aarninkhof et al.* (2005a); *van Dongeren et al.* (2008)) han ocupado imágenes ópticas de larga exposición de olas en rotura para estimar patrones que son utilizados como los de disipación. Así, obtienen estimaciones de batimetría en base a comparaciones entre las observaciones y predicciones de modelos. Este enfoque ha tenido menos atención debido a que carece una base física para estimar la disipación, ya que la señal está contaminada por otras que emergen de otros fenómenos, como la espuma remanente. También se han desarrollado métodos híbridos. Estos son capaces de conjugar los anteriores y otras variables que pueden depender del fondo de maneras más complejas. Por ejemplo, *Wilson et al.* (2014) usaron mediciones remotas de celeridad y corrientes, a través de métodos de asimilación de datos, y obtuvieron buenos resultados.

En este trabajo se presenta una metodología para estimar la batimetría costera a partir de campos de disipación por rotura obtenidos remotamente con el método de *Díaz et al.* (2017), quienes lograron aislar la señal de espuma remanente y cuantificar la disipación ola a ola. Esta variable es incorporada a un modelo de propagación de oleaje a través de un sistema de asimilación de datos que trata a la batimetría como un parámetro incierto, condicionado a las observaciones cada vez que estas están disponibles.

A partir de una estimación inicial, que incluye muy poca información sobre la morfología real, los resultados muestran que esta metodología es capaz de recuperar con bastante precisión la ubicación y amplitud de una barra de arena y su interrupción por un canal de retorno, propios de la playa en estudio. Estos resultados incentivan aplicaciones donde la batimetría costera pueda ser monitoreada continuamente sin necesidad de mediciones directas de profundidad.

Palabras Claves: *inversión batimetría, disipación energía por rotura, asimilación de datos.*

Abstract

Bathymetry is a fundamental parameter for the prediction of wave propagation and coastal currents, yet it is often unknown and hard to measure.

Fortunately, as the influence of bathymetry on many coastal processes is fairly well understood, it is possible to pose an inverse problem, i.e., bathymetry inversion. In the last decades, mainly to the outspread of digital cameras and other remote sensors, two main dependencies have been exploited: wave celerity and wave breaking dissipation (*Holman and Haller* (2013)).

The former (e.g. *Holman et al.* (2013)) uses signal processing techniques to estimate the wave's phase speed and invert the linear dispersion relation to estimate depth. While showing good performance outside the surf zone, their accuracy degrades shoreward due to wave nonlinearities (*Catalán and Haller* (2008)) and the spurious acceleration measured by remote sensors when the imaging mechanism changes as waves break (*Brodie et al.* (2018)). Others (e.g. *Aarninkhof et al.* (2005a); *van Dongeren et al.* (2008)) have used long exposure optical images of breaking waves to estimate patterns that are treated as dissipation proxies. Inverted depths are then obtained in light of the difference between measurements and model predictions. This approach has had less attention, possibly due to the lack of a physical background to estimate dissipation, as this signal is contaminated by that arising from other phenomena such as remnant foam. Lately, hybrid methods have been developed too. These are capable of combining the previous and other variables that may depend on depth in intricate ways, using data assimilation tools. For instance, *Wilson et al.* (2014) used remote measurements of celerity and alongshore currents with very good results.

This work presents a methodology to estimate nearshore bathymetry from remote measurements of wave breaking dissipation following *Díaz et al.* (2017), who were able to remove the remnant foam signal, and reliably estimate breaking dissipation on a wave by wave basis. Two-dimensional dissipation fields are then introduced in a data assimilation scheme that treats bathymetry as an uncertain model parameter, which is conditioned to dissipation measurements every time they are available.

Starting from an initial estimate that includes little information about the true morphological state, results show that this system is able to estimate with good accuracy three-dimensional features such as nearshore sandbars and rip channels. These results suggest applications where nearshore bathymetry could be continuously monitored only from remote sensing data.

Keywords: *bathymetry inversion, wave breaking dissipation, data assimilation.*

Glossary

$0_{m\times n}$	Null matrix $\in \Re^{m\times n}$
A	Roller cross-sectional area
α	Wave direction relative to the cross-shore axis, positive CCW
c	Wave phase velocity
$C_{\epsilon\epsilon}$	Measurement error covariance
$C_{\psi\psi}$	Model error covariance
D_{br}	Time averaged rate of wave breaking energy dissipation
D_r	Time averaged rate of roller energy dissipation
$D^{obs}_{t_i}$	Measured roller dissipation at time t_i
D^f	Model predicted roller dissipation
EnKF	Ensemble Kalman Filter
ϵ	Measurement perturbations
E_r	Roller energy
g	Gravitational acceleration
h	Bathymetry
H_{m0}	Significant wave height
I	Uncalibrated optical intensity
$JPDF$	Joint probability density function
k	Wave number
L, M	Linear interpolators
l^{obs}_c	Observations localization range
l^f_c	Model covariance localization range
L_r	Along slope roller length
L'_r	Roller lenght projection in the horizontal plane, along the wave propagation direction
L_x, L_y	Horizontal lenght scales
N	Ensemble size
Ω	Localization function
pdf	Probability density function
ψ	State vector
Q	Process error
ρ'	Roller mass density
ρ	Matrix arrangement of the localization function
σ	Wave frequency
σ_0	Radar backscatter
σ_z	Bathymetry ensemble standard deviation
$SWAN$	Simulating waves nearshore
$\bar{\tau}$	Tangential stress
T	Wave period
θ	Roller front slope angle
U	Depth averaged current

Contents

List of Figures

Chapter 1

Introduction

The nearshore is the geographical band where oceans and lands interact. In spite of its limited extent, it is one of the areas humans show most concern for, as several activities take place there, ranging from recreational to political and economic, and also provides protection againts environmental hazards that may affect hinterland.

From a scientific point of view, the nearshore is an extremely dynamic environment characterized by the interaction of hydrodynamic and morphodynamic phenomena over a wide range of spatial and temporal scales. Wave breaking and currents induce sediment transport reshaping the coastal morphology. In turn, these bathymetric changes provide feedback to the wave field, modifying it and eventually inducing continuous changes (*Komar* (1998)).

Hence, a good understanding and suitable prediction capabilities of the nearshore are interesting not only from a scientific perspective but also to the general interest of society, with the eventual long-term goal of improving management and increasing safety.

Fundamental for these purposes is an accurate representation of bathymetry. Good estimates of underwater topography, in addition to reliable numerical models, might improve present prediction capabilities (e.g. *Wilson et al.* (2010)). This approach treats bathymetry as an input, and as such, is usually called a *forward problem*. However, bathymetric estimates at hand usually lack the spatial and temporal resolution required, as they are not always measurable at the required operational rates and safe conditions. Sometimes they are completely absent, and users are forced to assume some reasonable beach shape.

Fortunately, as the influence of bathymetry on many coastal processes that have strong signatures on remote sensors, such as wave propagation and coastal currents, is fairly well understood, it is possible to pose an inverse problem, i.e., *bathymetry inversion*. In the last decades, mainly driven by the outspread of digital cameras and other remote sensors, two main depth dependencies have been exploited: wave celerity and wave breaking dissipation (see *Holman and Haller* (2013) for a review).

The former (e.g. *Holman et al.* (2013)) uses signal processing techniques to estimate the phase propagation velocity and invert the linear dispersion relation to estimate depth. While showing good performance outside the surf zone, their accuracy degrades shoreward due to wave nonlinearities (*Catalán and Haller* (2008)) and the spurious acceleration measured by remote sensors when the imaging mechanism changes as waves break (*Brodie et al.* (2018)).

Others (e.g. *Aarninkhof et al.* (2005a); *van Dongeren et al.* (2008)) have used long exposure optical images of breaking waves to estimate patterns that are treated as dissipation proxies. Inverted depths are then obtained in light of the difference between measurements and model predictions. Although wave breaking is the dominant process in the surf zone, this approach has had less attention, possibly due to the lack of a physical background to estimate dissipation, as this signal is contaminated by that arising from other phenomena such as remnant foam or steepening waves.

Lately, hybrid methods have also been developed. These are capable of combining the several variables that may depend on depth in intricate ways, using data assimilation tools. For instance,

Wilson et al. (2014) used remote measurements of celerity and alongshore currents with fair results in the surf zone. Yet, one potential downside is the need to couple in situ data to estimate these more complex variables, and thus to drive the assimilation. This can affect the benefit of having a purely remote sensing based estimate.

This work intends to bridge this gap, namely a reliable method for the estimation of surf zone depths from remote sensing data. Here a data assimilation approach treating bathymetry as an uncertain model parameter is introduced where direct dissipation estimates from remote sensing data are the unique data source. Two-dimensional wave breaking dissipation fields are retrieved on a wave-by-wave basis with the algorithms of *Díaz et al.* (2017), who were able to reliably estimate breaking dissipation by removing spurious signals affecting electro-optical and microwave data.

The crux of the data assimilation approach is that it uses a model to compute predictions, and then it conditions the predictions given the information contained in the observations. Herein, following *Wilson et al.* (2014), bathymetry is treated as the only source of model error. This is a simplifying assumption but is supported by the fact that bathymetric uncertainty often dominates model errors.

This thesis is structured as follows. Chapter 2 presents a literature review regarding existing bathymetry inversion techniques. This is followed by the statement of the present objectives and hypothesis in chapter 3. Chapter 4 presents the methodology of this work. This includes an overview of the remote sensing product used and the inversion system to which it is passed. The system is tested against in situ data from a field experiment conducted at Duck, NC, and its results and analysis are shown in chapter 5, along with their discussion in chapter 6. Finally, conclusions are formulated in chapter 7.

Chapter 2

Literature review

2.1 Introduction

The dynamic nature of bathymetry is a major factor for surf zone behaviour and evolution. Significant bathymetric changes can occur rapidly, even on time scales of less than one day (*Lippmann and Holman* (1990)). In fact, bathymetric uncertainty has been demonstrated to be one of the dominant parameters in model errors (e.g. *Wilson et al.* (2010); *Allard et al.* (2008)). As a result, good estimates of underwater topography, in addition to reliable numerical models, might improve present predictive capabilities. This approach, that treats bathymetry as an input, is usually called a *forward* or prediction problem.

However, bathymetric estimates at hand usually either lack the spatial and temporal resolution required, it is not directly measurable at operational rates and safe conditions, or it is at all unknown. In situ instruments, for instance sonar altimeters (*Gallagher et al.* (1996)), provide punctual estimates of seafloor elevation every few minutes with centimeter accuracy. Jetski (*Dugan et al.* (2001a)) and bottom-contacting vehicle surveys (*Birkemeier and Mason* (1984)) have high spatial resolution but are time consuming and not safe to operate during storms, when more bottom variability is expected. On the other hand, for clear waters remote sensors can yield direct estimates of depth, for example, by taking advantage of the radiative transfer of light into water and its interaction with the seafloor (*Mobley* (1994)) or with laser ranging techniques (*Irish and Lillycrop* (1999)). Yet, this condition is rarely met on natural beaches.

Fortunately, as the influence of bathymetry on many nearshore processes that have strong signatures on remote sensors, such as wave propagation and coastal currents, is fairly well understood, it is possible to pose an inverse problem, *bathymetry inversion*. This is roughly a two step process. First, a quantity different than depth is measured. Second, using a proper transfer function, the bathymetry that would reproduce the observed properties by solving the forward problem, can be estimated. In this regard, inversion methods can be differentiated by the measured property and by the nature of the transfer function used.

In this chapter bathymetry inversion methods based on remote sensing are briefly reviewed. The foccus is on the main hypotheses used, why they are challenging to be applied in the surf zone, and how the product used in this work could fill that gap.

2.2 Bathymetry inversion

Bathymetry inversion is a relatively young concept. In fact, first documented efforts are related to World War II, when the interest was in remote estimations of depth and surf zone conditions for safe military landings (e.g. *Williams* (1947)). Series of aerial photographs of the free surface were used to estimate wave numbers and frequencies from which depth could be obtained with the linear dispersion relation. With its inherent drawbacks and inaccuracies this method set a precedent, and some of the recent methods still take advantage of this idea.

Since then, and mainly due to the outspread of digital cameras and other sensors in the last decades, two depth dependencies have been exploited: wave celerity and wave breaking dissipation (see *Holman et al.* (2013) for a review). The former, here arbitraly called dispersion relation methods, will be presented first, followed by dissipation methods. Novel hybrid approaches are discussed thirdly.

2.2.1 Dispersion relation methods

As mentioned, this group of methods exploit the wave phase velocity depth dependence that can expressed in the form of a dispersion relation. Following *Dean and Dalrymple* (1991), the dispersion relation that stems from linear wave theory reads:

$$\sigma = \sqrt{gk\tanh(kh)} + \mathbf{U}\cdot\mathbf{k}, \tag{2.1}$$

where σ is the wave frequency, g the gravitational acceleration, k the wave number magnitude, h depth, and $\mathbf{U}$ the vertically averaged current vector. In general, $\mathbf{U}$ has a vertical structure that could be accounted for by means of approximate formulations (e.g. *Kirby and Chen* (1989)). Yet such an approach remains challenging to be applied for bathymetry inversion owing to the dependence of $\mathbf{U}$ on the full vertical current profile which is often unknown. Instead, it is presumed as depth uniform (e.g. *Honegger et al.* (2020)). Besides, on open beaches, the depth-averaged current is usually considered negligible compared to the phase speed, so the Doppler shift term on the right-hand side of equation 2.1 is dropped (e.g. *Holland* (2001)). This implies that for estimating h, wave frequency and the space-varying wave number are needed. Remote sensors like video cameras and X-band marine radars are well suited for this, as their signals have proven to capture useful sea surface signatures, in addition to their favorable temporal and spatial coverages to retrive σ and $\mathbf{k}$.

At least three ways to estimate $(\sigma, \mathbf{k})$ pairs from these sensors exist, namely: cross correlations in time and space (e.g. *Bell* (1999); *Almar et al.* (2009, 2019)), cross-spectral (e.g. *Stockdon and Holman* (2000); *Plant et al.* (2008); *Holman et al.* (2013)), and three dimensional Fourier transform methods (e.g. *Dugan et al.* (2001b)).

The latter have shown to degrade near shorelines due to wave inhomogeneities in shallow waters (*Rutten et al.* (2017)) and its need for big analysis tiles, i.e., spatial sampling windows of order $O(100m)$, to keep uncertainties low (*Piotrowski and Dugan* (2003)). Also, its rough resolution misrepresents smaller bathymetric features expected in surf zones (*Plant et al.* (2008)). So, Fourier transform methods will not be further considered here.

The first two are similar, indeed under monochromatic wave conditions they are equivalent given the inverse relation between temporal and spectral correlations (*Bendat and Piersol* (2010)). In addition, using synthetic data, *Bergsma and Almar* (2018) showed minimal differences between them in the case of a JONSWAP spectrum. So, in the following discussion, they are dealt jointly. Recently *Simarro et al.* (2019) also developed a method to estimate $(\sigma, \mathbf{k})$ pairs pairs from optical data. Their approach is close in spirit to cross-spectral methods but uses slightly different mathematical tools (Hilbert transforms) and retrieves comparable results, so they would not be inspected in detail here.

The cBathy algorithm (*Holman et al.* (2013)) is probably the most widespread procedure for bathymetric inversion among the scientific community. It was originally developed for optical videos from Argus cameras (*Holman and Stanley* (2007)), but has also been applied to unmanned aerial vehicles (e.g. *Holman et al.* (2017)), and adapted to X-band marine radar measurements

(*Honegger et al.* (2019)). cBathy is a cross-spectral method that operates over analysis tiles of order $O(10m)$. By considering the most coherent (usually four) frequencies in the surface wave band, cBathy computes their wave numbers through a non-linear fit to a sinusoidal model for spatial phase, and estimates depth via a second non-linear fit of these $(\sigma, \mathbf{k})$ pairs to equation 2.1. Objective error estimates are also given as 95% confidence intervals of the final fitting. In a third step, estimates are pointwise Kalman filtered every time new data are available (*Kalman* (1960)).

Under mild energetic conditions (significant wave height $H_{m0} \leq 1.5m$) initial retrievals were found fair in comparison to field surveys. Absolute bias and root mean square error were smaller than $0.5m$ and $0.8m$ respectively, averaging from the shoreline up to $500m$ offshore at a North Atlantic beach near Duck, NC (same site as this study). In the cross shore direction the errors ranged from seaward underestimations to shoreward overestimations of depth (see *Holman et al.* (2013) figures 5 and 6). However, the ratio of observed to estimated error after Kalman filtering was slightly more than 7. *Honegger et al.* (2019) found similar bulk performance and error depth dependence when applying cBathy to X-band observations.

Recently, *Brodie et al.* (2018) evaluated cBathy performance over a wider range of offshore wave conditions, comparing its retrievals against vessel surveys and in situ altimeters. Their main results showed poor performance with waves higher than $H_{m0} > 1.2m$, and when breaking took place over an offshore bar. Specifically, depth overestimations near and offshore of the sandbar and underestimations on its shoreward face and trough were attributed to a mismatch between linearly predicted and measured celerities (discussed next). They reported a systematic bias, dependent on wave height and water depth, that is not in agreement with the confidence interval provided by the algorithm. *Bergsma and Almar* (2018) found similar error behavior. In addition, the effectiveness of the Kalman filter was evaluated, and showed its inhability to filter biased estimates after storms. Still, cBathy was proved to be accurate during low energy conditions.

The work of *Haithuan et al.* (2019) also tested the performance of a dispersion relation method, but instead of using in situ depth measurements they proposed a novel approach based on tidal elevations. Their method stems from comparing the video-based tidal signal, calculated as the difference between the instantaneous inverted depth and a 3-day moving average of it, to the tide level measured by a nearby gauge.

Using a three year long data set, *Haithuan et al.* (2019) were able to quantify the inversion error (spatial and seasonal variability) at Nha Trang beach in Vietnam, and visually decomposed three types of error inherent to dispersion relation methods, namely: deep water limitation, breakpoint optical effect and nonlinear effects, which are consistent with the results of the studies mentioned above.

The deep water limitation is a physical constraint that bounds the offshore coverage of these methods. As waves propagate to shore they are said to start feeling the bottom when $kh < \pi$ (*Dean and Dalrymple* (1991)). When this condition is not met the hyperbolic tangent in equation 2.1 becomes one and the depth dependence is lost. Thus, limiting the applicability of the dispersion relation under short wave forcing. This is particularly restrictive in regions where the sea state is most of the time composed of wind waves or in sheltered areas. Operationally, there is also the possibility that the sensor resolution gets too coarse in the offshore direction, not allowing to resolve short waves.

On the other side, shoreward of the breakpoint waves propagate with a bore-like shape and nonlinearities become prominent (e.g. *Guza and Thornton* (1980); *Thornton and Guza* (1982)). *Holland* (2001) showed a systematic overestimation bias in surf zone inverted depths (nominally $h < 4m$ at the same site of this study) when the linear dispersion relation is used, and that the offset increased with increasing wave heights. Thus, in accordance with finite amplitude effects. Further, *Catalán and Haller* (2008) corroborated that a composite dispersion relation, including nonlinear effects, reduced surf zone inversion errors to $O(10\%)$. Also, using laboratory data, *Almar et al.* (2011) showed that inversion algorithms are improved when using nonlinear models for wave celerity and wave heights. Unfortunately, remotely sensed estimations of wave breaking heights (e.g. *Almar et al.* (2012); *Andriolo et al.* (2020)) have not been included in field studies yet.

The breakpoint issue is not explained by water wave mechanics alone. Non breaking waves approaching a beach are visible in the optical band due to specular reflection of the sky radiance.

The observed reflected radiance is dependent on the Fresnel reflection coefficient that is in turn modulated by the free surface slope and the view direction. In the optical band, when viewing from shore, this makes the wave shoreward face appear dark and the seaward face bright. In contrast, as waves break the optical signal gets brighter in the front face due to the roller diffusive reflectivity (*Catalán et al.* (2011)). This forces a 180° phase shift in the modulation transfer function (*Stockdon and Holman* (2000)) and creates an aparent acceleration near the breakpoint that is undiscernible for current algorithms. *Brodie et al.* (2018) retrieved celerities up to three times greater than predicted with linear theory over the bar, and slightly smaller in the trough region, somehow indicating the opposite effect. This drawback is expected to influence radar based inversions in a lesser extent, as X-band electromagnetic waves interact differently with the water surface, showing higher backscatter near the wave crest before and after breaking (*Honegger et al.* (2019), *Catalán et al.* (2014)). However, this radar asset is hard to evaluate as the breakpoint error is mixed with nonlinear effects.

Lastly, an aspect rarely mentioned is that the dispersion relation 2.1 is derived from linear wave theory that, aside from the supposition of small amplitude and others hardly met in the surf zone, assumes a flat bottom. This can be interpreted the other way around, i.e., bottom variations considerably smaller than the wave height and length do not affect waves, and variations of greater scales should occur over various wave lenghts so waves have enough time and space to react linearly. This makes the understanding of dispersion relation methods hard, as it is unclear how the wave phase speed spatially reacts to sharp gradients or features of similar scales as sandbars.

2.2.2 Dissipation methods

The process of wave breaking involves several spatial and temporal scales, ranging from wave motions in the order of meters to small scale turbulence. In numerical models, these inherent complexities are treated by introducing ad-hoc parametrizations in the mass and momentum conservation laws to reproduce the onset, decay phase and cessation of breaking. For instance, the bore (e.g. *Battjes and Janssen* (1978); *Thornton and Guza* (1983)) and roller (e.g. *Svendsen* (1984); *Lippmann et al.* (1996)) approximations are used in phase averaged models with fair succes, in terms of root mean squared wave height and set-up, over natural profiles.

In spite of the numerous studies related to wave propagation and breaking on beaches, this depth dependence has had less atention than dispersion relation methods in the field of bathymetry inversion, at least with regard to the number of publications. The drawback is not only attributable to the complexity of the breaking process by itself, but also and most probably, to the difficult task of relating remote signals to geophysical quantities of interets, i.e., wave breaking energy dissipation.

The work of *Lippmann and Holman* (1989) can be considered a pivotal publication in this regard. They showed that the relation between sea surface optical signal and the underlying morphology could be established through time exposure images, thus removing wave height modulations and retaining the breaking paterns of wind and swell waves over a barred beach. While not actually measuring dissipation, their main result was that observed cross shore profiles of time averaged pixel intensities show good agreement with modeled dissipation over a mesured bottom profile. This opened up the posibility to infer bathymetry using dissipation as a proxy. Further, this relation allowed estimations of sand bar position and improved assesment of beach morphology and its spatial and temporal variability for video (*Lippmann and Holman* (1990); *van Enckevort et al.* (2004)) and radar (*Ruessink et al.* (2002)) measurements. However, as mentioned by the authors, the breaking patterns imaged in time exposures are contaminated with residual foam that remains floating at the water surface after breaking.

Taking into consideration the concept of wave roller and its effects on the optical signal, *Aarninkhof and Ruessink* (2004) developed a heuristic model to isolate the roller contribution from that arising from residual foam in timex images. Their image processing algorithm, after removal of background illumination, isolates the roller signal by multiplying the time-averaged intensity signal by a space varying reduction factor that depends on a nondimensional parameter representing the foam persistence on the sea surface. This parameter is estimated with an empiri-

cal relation between standard timex and variance images collected by the Argus system (*Holman and Stanley* (2007)). While showing good agreement between the isolated roller optical signal and modeled roller dissipation (*Stive and De Vriend* (1994)), in terms of peak locations and widths, their technique is based on two main assumptions: the shape of the time-averaged intensity signal (assumed as Gaussian bumps over sand bars), and that over time the roller related intensity lasts a half wave period. But most notably, the multiplying factor operates over time averaged cross-shore transects of pixel intensity, thus locally reducing the signal and not taking into account that it can be spatially shifted due to the presence of foam.

The work of *Aarninkhof et al.* (2005a) followed this idea and estimated dissipation by scaling the normalized roller signal with the incoming wave energy flux and compared it to model predictions to estimate bathymetry. Their inversion method is based on sediment fluxes between the seabed and a virtual buffer layer that controls the sediment's availability and distribution. The sediment conservation equation was set up in a way that a positive difference (modeled dissipation greater than observed) induced bed erosion and vice versa. After a yearlong application at Egmond, The Netherlands, this procedure showed good results on two cross shore profiles. Including the shoreward migration of an outer bar and the net sediment gain in the profile. The depth root mean squared errors were $\sim 0.2m$ over the bar and $\sim 0.6m$ in the trough region, biased deep and shallow respectively. The latter attributable to remnant foam, i.e., spurious observed dissipation causing seafloor rise. However, *Aarninkhof et al.* (2005a) technique performance depends on ad-hoc terms and a set of free parameters that control the sediment fluxes, redistribution and morphological time scales, and it is not clear how these are related to field conditions. As mentioned by the authors, the values they adopted are likely not the optimal for other sites. Thus, making the procedure uncertain to implement elsewhere.

This dissipation quantification methodology has also been applied to iterative assimilation schemes to infer bathymetry without morphological laws and with a slightly rougher image processing algorithm; simply scalling by offshore wave energy flux after removing background illumination. For instance, *Monfort and Lippmann* (2011) incrementally updated multiple cross shore profiles based on the difference between observed and modeled dissipation until convergence and *Aarninkhof et al.* (2005b) extended their original work to 2DH. While showing fair skill in their test cases, this method assumes that observed dissipation is the actual dissipation, thereby ignoring observational errors. This issue is treated more carefully in Beach Wizard, an assimilation algorithm that uses scalled timex images as proxy for roller dissipation as one of its data streams (*van Dongeren et al.* (2008)). This concepts will become apparent in the next section.

Finally, before moving to the next set of methods, it is important to mention the recent work of *Díaz et al.* (2017). They proposed a method to estimate two-dimensional wave breaking dissipation fields from remote sensing data. Their method stems from wave-resolving remote measurements of the sea surface used to estimate roller lengths in the wave's propagation directions, that are then coupled to *Duncan* (1981) model for rollers in equilibrium to estimate wave breaking dissipation on a wave-by-wave basis. In contrast to previous efforts (e.g. *Aarninkhof and Ruessink* (2004)), this approach has a physical background, as it reliably removes spurious breaking signals such as remnant foam. Its results showed good correlation in both structure and magnitude in comparison to a model prediction, and allowed the observation of a rip current location. As such, it opens up the possibility to implement a bathymetry inversion algorithm to be fed with its dissipation fields. As *Díaz et al.* (2017) work is fundamental for the present purposes it will be revisited in detail in chapter 4.

2.2.3 Hybrid methods

Both previously discussed methods lean on relations that link depth to the measured quantity in a one-variable fashion. For instance, the linear dispersion relation links depth to celerity and disregards any other depth dependence. This is just a modeling artifact, as in reality variables are obviously related through multiple hydrodynamic processes taking place in the surf zone. An inversion methodology able to incorporate multiple data sources is attractive as it could benefit from various depth dependencies and provide more robust estimates.

This was first attempted in Beach Wizard (*van Dongeren et al.* (2008)), an assimilative algorithm that updates depth based on the difference between observations and model predictions. It is able to process roller dissipation, cross shore celerity and intertidal topograhpy, following *Aarninkhof et al.* (2005b), *Stockdon and Holman* (2000) and *Aarninkhof et al.* (2003), respectively. After locally retrieving depth from each data source the algorithm combines them with a previous estimate through a sequential Kalman-like filter (*Bouttier and Courtier* (1999)) and produces a least squares estimate for h. Uncertainties needed for the filter are estimated as a standardized sum of the measurement error and the model-data mismatch. The reported application at Duck, NC, showed fair results after running for 10 days starting with an outdated bathymetry; root mean squared error droped from $0.8m$ to $0.3m$ over the same domain as cBathy. However, a detailed review of its cross shore performance when $H_{m0} > 1.5m$ shows improvements over the sandbar and worsenings in the trough region, attributable to breaking waves over the bar and remnant foam respectively (See *van Dongeren et al.* (2008) figure 6).

The Beach Wizard approach methodologically fails in some aspects that can be better dealt with. First of all, it requires that the measured variables are transformed to depth before assimilation. This is done through the so called tangent-linear equations, i.e., the derivative of the observed variables with respecto to depth. To do so, models are needed to analytically relate measurements to depth. The dispersion relation 2.1 was used for celerity, and for the roller dissipation the organized wave dissipation of *Baldock et al.* (1998) was used as a proxy. This introduces the systematic biases disscused in previous sections. Also, nonlocal influence of measurements was neglected in consideration of the high spatial resolution of the measurements. However, this should be particulary relevant in the case of dissipation, as along a wave ray dissipation has a spatial correlation which is not entirely accounted for by localy updating bathymetry (*van Dongeren et al.* (2008)). In any case, Beach Wizard proved the usefulness of the model-data assimilation approach to derive accurate bathymetries and its error estimates.

Using the same observed variables and adjoints *Birrien et al.* (2013) computed bathymetric cross-shore transects assimilating synthetic data, delocalizing updates with an ensemble approach. Similar to Beach Wizard, their nonlocal updates led them propose to use different observations across shore. Specifically, the methodology showed good skill when dissipation was used over the sandbar and celerity elsewhere.

A more formal data assimilation procedure is the one followed by *Wilson et al.* (2014), who implemented an ensemble Kalman filter (*Evensen* (1994a); *Burgers et al.* (1998), abbreviated EnKF), to infer bathymetry based on various remote observations. Their work widened the spectrum of depth dependencies for remote bathymetric inversion by assimilating remotely sensed wave number frequency pairs, alongshore currents and shoreline position, following *Holman et al.* (2013), *Chickadel et al.* (2003) and *Plant and Holman* (1997) respectively. This methodology showed excellent skill and retrieved improved estimates of bathymetry and surf zone circulation, including the prediction of a morphologically controled rip current (*Haller et al.* (2014)).

The main EnKF advantages in this context are its ability to be fed with multiple observations, that do not need to be transformed to depth, and that it manages uncertainties with an ensemble representation of the system state, also automatically allowing nonlocal updates. This means making statistical rather than analytical inversions based on simplified depth dependencies. As this is the procedure to be followed in this work, it will be presented in detail in the next chapter.

It is to note that data assimilation is by itself an ongoing field of research, and its specifics hinge on the particular aspects of the application (e.g. model linearity and dimensionality, number of measurements, error statistics). As such, several approaches might be applied for nearshore bathymetry inversion. For instance, *Wilson et al.* (2010), *Wilson et al.* (2014) and *Moghimi et al.* (2016) applied the ensemble approach, while others have implemented variational schemes (e.g. *Kurapov and Özkan-Haller* (2013); *Wilson and Berezhnoy* (2018)), both well documented in the seminal books of *Evensen* (2009) and *Bennett* (2002) respectively. Even novel schemes have been proposed (*Ghorbanidehno et al.* (2019)). An exhaustive inspection of previously used data assimilation algorithms and results is out of the scope of this literature review. The point to be acknowledged here is the EnKF ability to manage multiple data sources that relate to depth in complex ways, as the goal of the present work is to test a new remote product rather than the

performance of a specific assimilation algorithm.

2.3 Summary

Remote sensing of sea surface signatures has proven to be a useful tool for nearshore bathymetry inversion. Some algorithms are now being applied to quantify beach morphological evolution and its seasonal variability againts enviromental conditions (*Bergsma et al.* (2019)). However, some of its features still require attention, specifically over bars and trough regions. In this chapter, the principal methods applied to depth inversion have been reviewed.

Dispersion relation methods are more widely applied, probably as their formulation is straight forward given the link between celerity and depth in the form of dispersion relations. However, their results are inaccurate where linear wave theory breaks down and when the breaking process modifies the imaging mechanism. This even makes error estimate non-physical, as it stems from the fitting skill to simple phase models (*Holman et al.* (2013)).

Dissipation methods should be able to retrive surf zone depths correctly as breaking is the dominant process taking place there. Yet, these have had less attention as the dissipation depth dependence is harder to express with a simple mathematic relation and because previous remotely sensed dissipation estimates lack of a physical basis.

Hybrid methods take advantage of various data streams, thus can account for more than one hydrodynamic process at a time and show good results. Data assimilation formalisms such as the EnKF release the need for simple expressions that relate depth to these processes, hence allowing assimilation of variables that are related to depth in intricate and nonlocal ways. Yet, a potential drawback of the data assimilation approach is the need for further model inputs, such as the wave forcing.

Finally, it bears to note that none of the inversion methods discussed in this chapter have included dissipation estimates as the ones proposed by *Díaz et al.* (2017), who were able to reliably isolate the roller signal from the one arising from other phenomena, such as remnant foam, and estimated dissipation on a wave-by-wave basis. This is attractive as depth-limited wave breaking is the dominant process taking place in the surf zone, therefore its inclusion should improve surf zone bathymetric estimates. Consequently, this work presents a method to include these estimates in a data assimilation system previously used for bathymetry inversion.

Chapter 3

Objectives

As mentioned in section 2.3, none of the previously developed bathymetry inversion algorithms have included physics based wave breaking estimates as the one proposed by *Díaz et al.* (2017). Consequently, this work objectives are the following.

3.1 General objective

- Computationally implement a data assimilation system able to retrieve surf zone bathymetry from remotely sensed two-dimensional wave breaking dissipation fields.

3.2 Specific objectives

- Estimate wave breaking dissipation fields from remote sensing data following *Díaz et al.* (2017).
- Formulate a method to objectively estimate the remote measurements uncertainty.
- Employ a suitable numerical model to predict wave breaking dissipation fields.
- Study the sensitivity of the methodology to its parameters.
- Quantitatively compare this work results against in situ surveyed bathymetry.

3.3 Hypothesis

Also, as argued by *Holman and Haller* (2013) direct measurements of dissipation are equivalent to measuring the nearshore mean flow forcing, i.e., nearshore circulation. It is then expected that the remote sensing product used in this work retrieves comparable bathymetric estimates to the results of *Wilson et al.* (2014), who assimilated observations of alongshore currents (among other variables). Taking this into account, the preceding objective is based on the following hypothesis:

- Assimilating remote sensing estimates of wave breaking dissipation alone is enough to retrieve improved estimates of surf zone bathymetry.

Nevertheless, it is important to mention that these and other methods should not be regarded as to compete against each other. Conversely, assimilation schemes as the one used here should facilitate their contribution.

Chapter 4

Methodology

In this chapter the procedure for bathymetric inversion from remotely sensed wave breaking energy dissipation is presented. The inversion system is based on a sequential ensemble-based data assimilation scheme, that treats bathymetry as an uncertain model parameter, which is conditioned to dissipation measurements every time they are available. This methodology largely follows the work of *Wilson et al.* (2014).

The fundamental steps of the procedure are outlined below and in figure 4.1:

1. An initial ensemble of N bathymetric realizations is defined for simulation time $t_i = 1$ by adding perturbations to a first or best guess bathymetry.

2. A forward numerical model, f, is applied to each h_j member of the bathymetric ensemble, i.e., for $j = 1, \ldots, N$, with fixed wave boundary conditions for time t_i. Model outputs D_j, i.e., wave breaking dissipation predictions, are used to augment ensemble members to form the background state ensemble $\{\psi_1^f, \ldots, \psi_N^f\}_{t_i}$ (superscript ^{f} simply denotes forward model quantities).

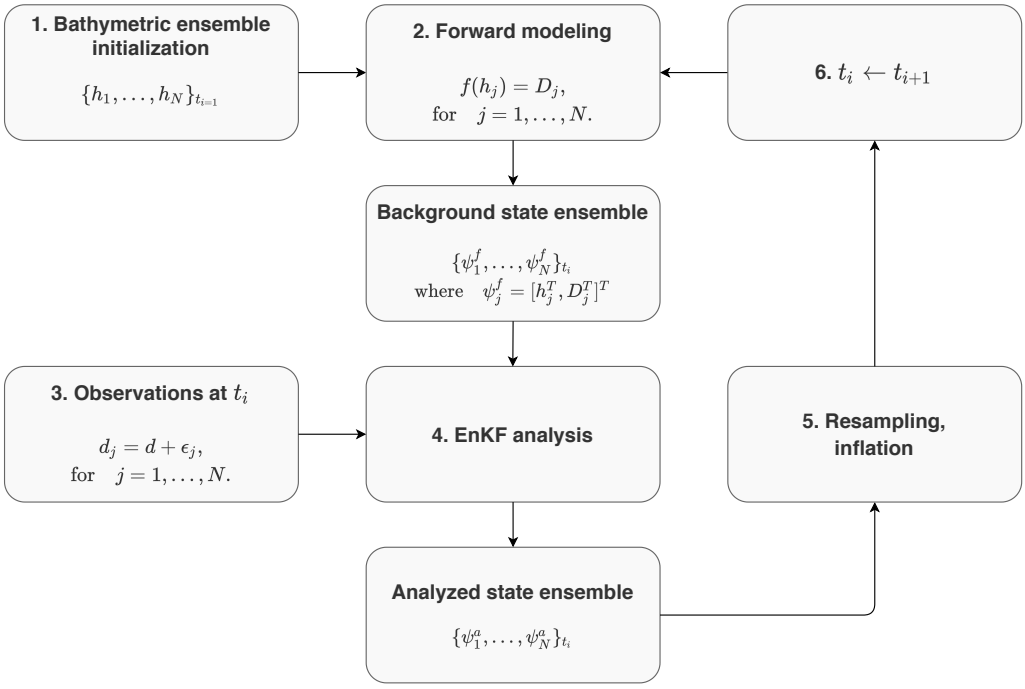

Figure 4.1: Bathymetry inversion system flowchart.

3. Corresponding remote measurements from time t_i are processed to estimate wave breaking energy dissipation along with its uncertainty, in the form of an ensemble of observations $d_j = d + \epsilon_j$, for $j = 1, \ldots, N$. Here d is the mean observed dissipation and d_j denotes random error fields.

4. Observations and model results are assimilated through the Ensemble Kalman Filter so that an updated or analyzed state ensemble, $\{\psi_1^a, \ldots, \psi_N^a\}_{t_i}$, is produced. Here ^{a} is for analysis.

5. To account for known filter shortcomings and unresolved sediment transport, the ensemble spread is adjusted and resampled to replace eventually failed members.

6. Before moving to the next observational time, by taking the proper rows of the ensemble matrix, inverted bathymetry and its uncertainty for time t_i are estimated as the ensemble mean and covariance respectively. Then, the cycle is repeated from step 2 for t_{i+1}, using the updated bathymetric ensemble.

As a result, several cycles of assimilation should retrieve improved estimates of bathymetry given the information provided by the observations and the model physics. In theory, cycles could be repeated infinitely and at each time step, the analyzed ensemble would be an updated system state that combines all previous information with current observations. On a practical level, however, some limitations may exist. For instance, this particular application is limited by daylight hours.

In the following, insight about the field experiment from which the data was adquired is given. This is followed by a revisitation of the retrieval algorithm of *Díaz et al.* (2017), used to estimate the wave breaking energy dissipation. Finally, the specifics of the inversion system are presented.

4.1 Data acquisition

Data was collected at the U.S. Army Corps of Engineers (USACE) Field Research Facility (FRF) near the town of Duck, NC, during the Surf Zone Optics experiment, on September 9th - 15th, 2010 (*Jessup et al.* (2012)). The study domain consists of about a $1km$ alongshore sandy beach, from the shoreline to $\sim 8m$ depth. A local cartesian reference system is used with its x axis pointing in the offshore direction and the y axis oriented in the alongshore direction, rotated 18° counterclockwise with respect to the geographical north. Vertical coordinates are relative to the NAVD88 datum. In figure 4.2 the reference system is shown, superimposed over a satellite image of the FRF. Locations of the remote and in situ sensors that are presented bellow are also indicated.

Figure 4.2: FRF site at Duck, NC, with local coordinate system and reference location of sensors (©2013 Google Earth).

4.1.1 In situ data

Around the time of the experiment two bathymetric surveys were conducted with the Light Amphibious Resupply Cargo (LARC), on 6 and 15 September. A standard survey consists of multiple cross-shore transects roughly separated by $50m$ in the alongshore direction. These data are used for validation of the bathymetry inversion procedure. For visualization purposes, raw data is bilinearly interpolated and smoothed for presentation.

For forward modeling purposes (section 4.3.4), measurements from the 8m-Array (*Long* (1996)) are used as wave spectral boundary conditions. This is a set of 15 bottom-mounted pressure sensors deployed approximately at $(x, y) = (900, 800)m$ (figure 4.2), at a nominal depth of $8m$. Measurements were processed to form estimates of frequency-directional spectra every $3h$.

Tidal elevations are also an input for the forward model. These are provided by the FRF NOAA Tide Station located at the tip of the FRF pier, approximately at $(x, y) = (600, 516)m$ (figure 4.2).

4.1.2 Remote measurements

The first system comprises three out of the five deployed cameras from the Argus station (*Holman and Stanley* (2007)), on top of a $43m$ tower located at $(x, y) = (32, 590)m$ (figure 4.2). Cameras looking to the north, northeast and east, labeled with the numbers 0, 3 and 1 respectively, are used (figure 4.3). The combined field of view covers the alongshore extent from $y = 500m$ to $y = 1000m$, and from $x = 60m$ to $x = 600m$ in the cross shore direction. Yet, only pixels where $y \geq 530m$ are considered to avoid the pier shadow. Pixel resolution naturally degrades with distance from the tower, ranging from $0.25m$ to $10m$. Cameras were setup to sample data at $2Hz$ for 17 minutes at the begining of every half hour during daylight hours.

Second, a radar was mounted over a $10m$ tower at $(x, y, z) = (17, 971, 14)m$ (figure 4.2). The marine radar is an active sensor with single polarization (HH) and $25kW$ nominal power operating at $9.45GHz$. Its $9ft$ antenna rotates at approximately $44rmp$, i.e., every point is sampled every $1.36s$. The system was configured to measure uncalibrated backscatter intensities in range bins every $3m$ upto $927m$ radialy, and in 270 azimuthal bins over approximately a 240° swath (figure 4.3). Relative azimuth and time records allow geolocation and synchronization. Data were collected on top of each hour for 17 minutes. Further details can be found in *Catalán et al.* (2011). Figure 4.3 shows assembled cameras and radar fields of view.

Raw data has to be preprocessed and interpolated to a common grid before it is fed into the dissipation quantification algorithms of *Díaz et al.* (2017). Raw camera imagery are rectified to an

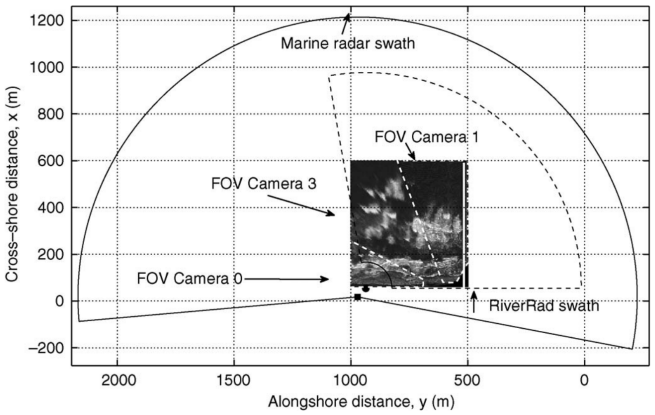

Figure 4.3: Remote sensors field of view. Circular sectors denote the swath covered by the marine radar (solid line) and RiverRad (dashed line, not used). White dashed lines bound cameras field of view, over a merged snap. Vertical white line at $y = 516m$ indicates the FRF pier. Figure originally from *Catalán et al.* (2011), p.1882.

horizontal plane at the mean sea level, and pixel intensities are interpolated to a uniform grid with resolution $\Delta x = 2m$, $\Delta y = 5m$. On the other hand, uncalibrated radar data is first transformed to normalized radar cross section (*NRCS*, σ_0 [dB]) following *Catalan* (2008) to remove its range and system dependence. Then, radar scans (helix surfaces in 3D time-space) are transformed to snaps by fixing each scan to its mean time and spatially interpolating to the new optical grid. Finally, video snaps are subsampled to radar times.

4.2 Quantification of surf zone wave breaking dissipation

The procedure proposed by *Díaz et al.* (2017) is based on the fusion of optical and X-band data to isolate the roller signal and capture its plan geometry. Then it is coupled to a physical model that estimates dissipation on a wave by wave basis. The main methodological steps of this procedure are presented next and, as it is fundamental for the present purposes, an estimate of the observational error is also given.

4.2.1 Surf zone sea surface characterization

To isolate the roller signal from remnant foam, and eventually other wave breaking false alarms, it is necessary to objectively characterize and classify the different sea surface stages present in the surf zone.

This is done following *Catalán et al.* (2011), who used an empirical statistical approach to distinguish different wave stages based on X-band and optical signals. They compared expected (from radiative theories) probability density functions (*pdf*) for the optical intensity (I) and radar

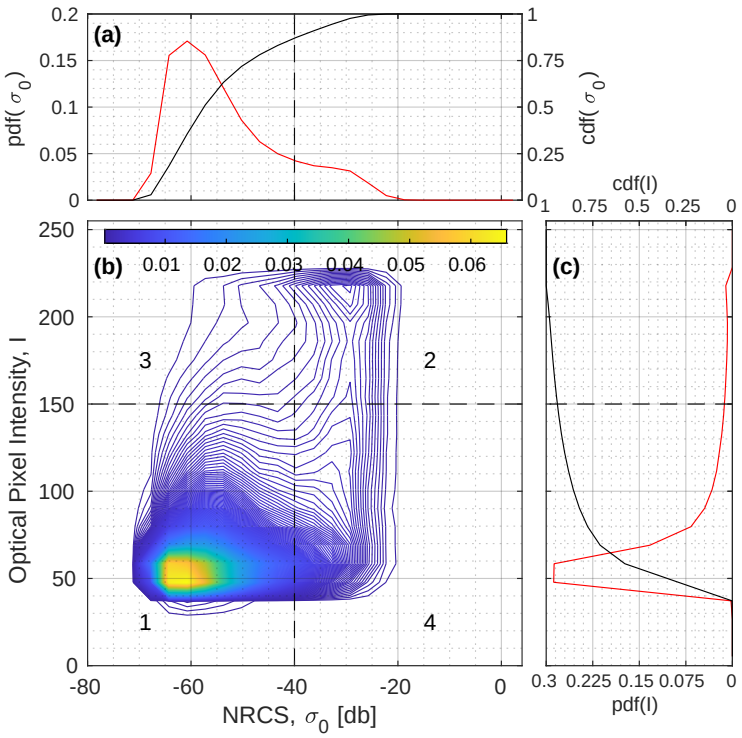

Figure 4.4: Sample *JPDF* and *pdf*'s of remote sensing data. Camera-0 at 14.59, 10th Sep. 2010. *pdf* of X band data (a), *JPDF* (b), and *pdf* of optical data (c). In (a) and (c) red and black lines are the marginal and cumulative probability density functions respectively. Black dashed lines across all subplots are the selected thresholds that divide the *JPDF* in four regions (numbers in panel (b)), corresponding to different wave stages (see text).

backscatter ($NRCS$, σ_0) to computed histograms over a variety of wave, wind and tidal conditions in the cross shore direction. Conclusions were that in the outer bar region the joint probability density function ($JPDF$), i.e., sensor fusion, provides sufficient information to discriminate pixels where active breaking is taking place. For the present dataset and wave conditions, the outer bar region is defined by $140 \leq x \leq 260m$.

As can be seen in figure 4.4(b), four distinct regions in the $JPDF$, associated with different wave stages, are identified from sensor fusion. Following the number labeling: nonbreaking waves, active breaking, remnant foam and steep waves. This statistical behaviour is explained by the individual imaging mechanisms of the sensors, noticeable in the marginal pdf's. The radar energy backscatter distribution (red line, panel (a)) shows an inflexion point at high $NRCS$ ($\sigma_0 \approx -30dB$), suggestive of departure from Bragg and composite surface theory scattering mechanisms, which is indicative of sea spikes (steepening and breaking waves). On the other hand, optical data (red line, panel (c)) peaks at low intensities due to wave slope modulations in specular reflection from nonbreaking waves, drops with higher intentities, and has a second peak that corresponds to the whitecap and foam diffusive reflectivity. Thus, each instrument is subjected to breaking false alarms, but simultaneous analysis allows discrimination of active breaking.

As a result, sea surface classification hangs on threshold selection. Following *Carini et al.* (2015), *Díaz et al.* (2017) implemented an automatized threshold selection algorithm based on the first and second derivatives of the individual pdf, which are discretely approximated to first order by,

$$pdf'(S_i) = \frac{pdf(S_i) - pdf(S_{i-1})}{S_i - S_{i-1}}, \quad \text{for} \quad i = 2, ..., N_t, \tag{4.1}$$

and

$$pdf''(S_i) = \frac{pdf'(S_i) - pdf'(S_{i-1})}{S_i - S_{i-1}}, \quad \text{for} \quad i = 3, ..., N_t. \tag{4.2}$$

pdf', pdf'' represent the first and second order derivatives of the pdf with respect to S, which is either signal, and N_t is one more than the number of bins used to compute the corresponding histogram.

The selection algorithm works as follows. The first zero of the first-order derivative is searched

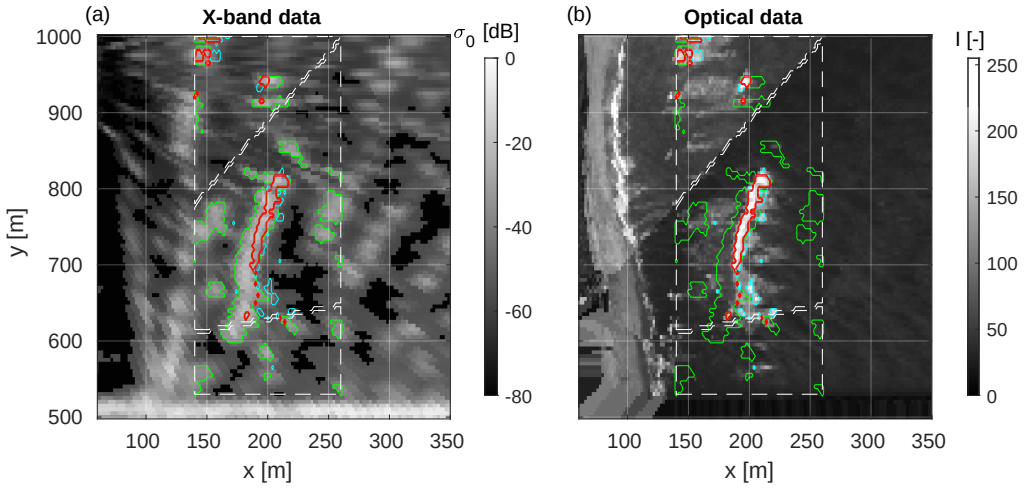

Figure 4.5: Breaking masks at 15:09:59, 10th Sep. 2010. Over radar backscatter (a) and uncalibrated optical signal (b), computed with the thresholds indicated in figure 4.4. Green, red and cyan lines confine steepening waves, breaking waves and remnant foam regions respectively. White dashed lines are cameras boundaries, limited in the cross-shore direction by the considered outer bar region.

at values greater than the maximum of the *pdf*,

$$pdf'(S^t) = 0, \quad S > S_{\max\,(pdf)}, \tag{4.3}$$

where S^t is the selected threshold and $S_{\max\,(pdf)}$ is the signal value that maximizes its *pdf*. If this condition is met, S^t marks the position of a *pdf* local minimum, predictive of a second peak at higher intensities. Conversely, if no local minima are found, the algorithm looks for the point of maximum curvature, indicative of a change of behaviour in the distributions. Approximating curvature with equation 4.2,

$$pdf''(S^t) = \max\left(pdf''(S > S_{\max\,(pdf)})\right). \tag{4.4}$$

This situation might happen under unfavourable conditions, like adverse weather, excessive foam production or sun glare (*Díaz et al.* (2017); *Catalán et al.* (2014)).

The final step of the threshold selection algorithm sets hard coded limits based on the data sets of *Catalán et al.* (2011). If the video intensity threshold falls out of the inverval $(70, 170)$, $2\bar{I}_{\max}/3$ is used, where $\bar{I}_{\max}$ is the maximum intensity of the timex image. In the same way, if the radar threshold does not result to be in the range (-28,-25) the algorithm assigns either limit. Nevertheless, for the present data set visual inspection was fundamental to fine tune the results.

Next, selected thresholds are used in the time domain to classify each pixel with one of four wave stages. Thus, discarding direct instrument measurements and building the so called breaking masks, which are binary three-dimensional matrices indicating the wave stage taking place in each pixel over time. Figure 4.5 illustrates a sample breaking mask over its corresponding marine radar and optical snapshots. As appreciated, the procedure is able to fairly recognize a wave with long crest (near $x = 200m$, between $y = 700m$ and $y = 820m$) but shows some speckles to the south of it ($y < 700m$), and has trouble identifing a unique wave roller at $(x, y) = (150, 980)m$ (or disregard spurious signals). As data assimilation highly depends on observational errors this will be further analyzed in the following sections.

Díaz et al. (2017) proposed a roller tracking method between snapshots that allows bookkeeping of its lagrangian trajectories, thus its propagation angle, α. The method relates two instances of the same roller in consecutive frames if their centroids propagate at a velocity smaller than a celerity threshold, $c_{thr} = \sqrt{c_x^2 + c_y^2}$, where c_x and c_y are user defined nominal wave celerity components, taken from linear wave theory assuming a $10s$ period wave in $10m$ depth.

The tracking technique allows instantaneous estimation of local roller lengths. In other words, for every pixel at the front of each roller, the roller length is estimated as the distance between the front and back pixel in the wave propagation direction. This measure is saved in a new matrix, here denominated $L_r'(x, y, t)$, which stores the instantaneous plan view roller length at the position of the front pixels and assigns zeros to all other grid points. The prime in L_r' is intended for differentiating this variable from the along slope roller length L_r introduced in the following section (figure 4.6).

4.2.2 Dissipation from roller geometry

In his early work, *Duncan* (1981) proposed a model for wave breaking dissipation for rollers in equilibrium. By integrating the vertical and horizontal momentum equations over the breaking region (2DV system, parallel to the cross wave direction as in figure 4.6), it was shown that the tangential component of the weight of the roller is balanced by the stresses acting on its interface with the subjacent wave. In symbols,

$$\rho' g A \sin\theta = \bar{\tau} L_r, \tag{4.5}$$

where ρ' is the roller mass density, g is gravity, A is the area of the roller in the vertical plane, θ is the roller inclination angle with respect to the horizontal, $\bar{\tau}$ is the mean shear stress and L_r is its along slope length. Values adopted for the roller mass density and its front slope angle are discussed in the folloeing section.

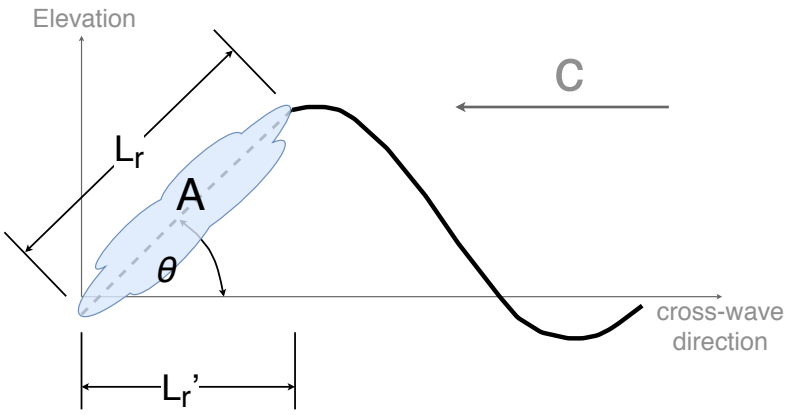

Figure 4.6: Schematic wave roller geometry. Elevation view in the cross-wave direction.

Dally and Brown (1995) used this formulation to estimate the rate of roller energy dissipation per unit planform area by multiplying equation 4.5 by the face speed c and dividing by the wavelength L. Consequently, the rate of roller energy dissipation can be written as,

$$D_r = \frac{\rho' g A \sin\theta \cos\theta}{T}, \tag{4.6}$$

where T is the wave period.

Equally important, *Duncan* (1981) experimental measurements indicated a roller geometry self-similarity through most of its life cycle,

$$\frac{A}{L_r^2} = 0.11 \pm 0.01. \tag{4.7}$$

As a result, *Díaz et al.* (2017) were able to estimate the rate of roller dissipation per unit planform area, by rearranging equations 4.5, 4.7 and considering geometry presented in figure 4.6,

$$D_r(x,y,t) = \frac{0.11 \rho' g L_r'(x,y,t)^2 \tan\theta}{T}. \tag{4.8}$$

When 4.8 is applied to a pair of optical and radar data recording (i.e., breaking mask), a time series of instantaneous dissipation maps is obtained. These fields are mapped on to the remote sensing grid by means of $L'(x,y,t)$. After time averaging over the record lenght at each individual grid point, *Díaz et al.* (2017) obtained time-averaged wave breaking dissipation fields, $D_{t_i}^{obs}(x,y)$, where the subscript indicates the observational time, and the superscript is intented for differentiating it from model predicted dissipation (section 4.3).

At this point a few conceptual remarks are given to clarify the previous derivation. Equation 4.5 states a force balance for a steady moving system, in accordance with *Duncan* (1981) experimental setup. Consequently, the equilibrium hypothesis and relation 4.7 are not necessarily met by waves approaching a natural beach. In spite of this, there are field and laboratory antecedents supporting this model (*Haller and Catalán* (2009); *Carini et al.* (2015); *Flores et al.* (2016)).

Next, equation 4.8 hides the assumption that all the dissipation takes place on the front of the roller. Physically this is unrealistic, but it is not clear how the wave by wave approach used to estimate dissipation relates to the computed dissipation by the phase averaged model from section 4.3.4. So, to keep consistency, 4.8 is used as it averages dissipation over the wave lenght, i.e., "phase averages", and it is assumed to occur in the front of the wave.

Finally, it is important to recall that the previous derivation is a wave-following derivation. Thus the estimated dissipation fields are Lagrangian quantities that are mapped to a common grid by time-averaging. This is a relevant observation, as model predictions used in the data assimilation framework are not derived with the same formulation. This will be further commented on in chapter 6.

4.2.3 Observational errors

As mentioned by *Holman and Haller* (2013) every remote sensing product should also deliver estimates of uncertainty. Unfortunately, the novel work of *Díaz et al.* (2017) does not provide error estimates. But, as this is mandatory for the present application, a heuristic approach is proposed to estimate the observational errors covariance.

As stated by the model 4.8, roller dissipation depends on the physical parameters ρ', T and θ and on the remotely sensed plan roller length L_r'. In reality, uncertainty in D_r depends on the quality of the values adopted for each one of these parameters. However, L_r' is the only directly measured quantity. Importantly, the same formulation is used in the roller module of the forward model (equations 4.20 and 4.21). Consequently, to estimate observational errors, ρ', T, and θ are used to propagate errors in L_r' into D_r. In the following values adopted for the first three parameters are justified, then the method used to estimate L_r' errors is explained.

First, on the lack of measurements for the roller mass density, it is taken to be 60% of the water density, based on *Duncan* (1981) discussion regarding the momentum deficit in the wake of the breaking region. This is a rough approximation, yet it is supported by previous applications of the roller formulation with remote sensing data (*Díaz et al.* (2017); *Carini et al.* (2015)).

Second, the peak wave period measured by the 8m-Array is used for T. While this might be a potential source of error, as it is acknowledged that incoming waves are not always narrow banded in frequency, in this context, this is supported by the following two facts. First, the detection algorithms of *Díaz et al.* (2017) are not yet capable of certainly differentiating waves by their period nor by their direction. Such an improvement would require further bookkeeping and processing of the Lagrangian history of each breaking wave, at a higher computational cost. Second, the forward model (section 4.3.4) also assumes that the spectrum is narrow banded in the frequency domain to compute roller related quantities. This decision, although consistent, might still introduce some error. Yet, the results shown in chapter 5 suggest that its influence is small.

The wave front slope angle, θ, is known to vary spatially and temporally as waves shoal and break. Based on a large experimental dataset, *Zhang et al.* (2017) reported values between 11° and 46° at the breakpoint, and proposed empirical formulas for its evolution given local wave parameters, the dimensionless depth and the bed slope. The application of these parameterizations is possible but would require approximations regarding bathymetry (the current unknown) and other wave parameters. On the other hand, the roller formulation in the forward model assumes a constant wavefront slope angle. Then, as a result, a constant θ value is used in space and time in 4.8. However, given the lack of knowledge regarding the true roller inclination angle, it is considered a tunable parameter whose influence is evaluated in chapter 6.

Consequently, observational errors are due to uncertainties in the measured roller lengths $L_r'(x, y, y)$, thus on thresholds selection. To consider this uncertainty a threshold variation scheme is proposed as follows. For each dataset, after computing the dissipation field, the selected thresholds, (I^t, σ_0^t), are varied every 5% within a ±15% of its selected value, uniformly over the images and time, and the procedure from sections 4.2.1 and 4.2.2 is repeated for each new threshold pair. Thus, at every observational time a set of 49 dissipation fields is generated, from which the observational error covariance is calculated as,

$$C_{\epsilon\epsilon}(\mathbf{x_1}, \mathbf{x_2}) = \Omega(|\mathbf{x_1} - \mathbf{x_2}|, l_c^{obs}) \cdot \mathrm{Cov}(D_{t_i}^{obs}(\mathbf{x_1}), D_{t_i}^{obs}(\mathbf{x_2})), \tag{4.9}$$

where $\mathbf{x_1} = (x_1, y_1)$ and $\mathbf{x_2} = (x_2, y_2)$ are the positions of sample points in the remote sensing grid, Cov is the sample covariance between two the sample points (from the 49 member set), and $\Omega(z, l_c^{obs})$ is a localization function that smoothly sets to zero covariances between points separated by distances z, greater than the double of a user-defined radius l_c^{obs} (introduced in detail in section 4.3.6).

The choice of a dynamical range of 15% for the thresholds is supported on visual inspection of the breaking masks against optical data. Thresholds outside this interval produce results with large errors, such as high rates of nondetection or oversized roller lengths. It is to note also, that preprocessing of radar data (conversion to NRCS, 4.1.1) theoretically removed its range dependence. Thus, supporting the application of the threshold variations over the whole image domain.

Also, the inclusion of the localization function is motivated by the fact that the covariance is calculated from a finite size ensemble of dissipation fields, which might induce sampling errors, i.e., correlation between distant points. This decision adds the localization range as a free parameter whose sensitivity will be discussed in the next chapters.

Finally, the threshold variation scheme is expected to produce coherent error estimates where the algorithm detects breaking waves. On the contrary, pixels where little or no breaking detection is observed, this scheme produces little or null variability. As will be exemplified in chapter 6, this situation is problematic for the inversion system. Therefore, a minimum variance equal to the square of the 10% of the maximum time-averaged dissipation is imposed on the covariance matrix 4.9. This is inspired by the measurement error introduced in Beach Wizard (*van Dongeren et al.* (2008)).

4.3 Bathymetry inversion system

In this section the methodology for assimilating dissipation observations in a steady state phase averaged wave model is described. Bathymetry is treated as an uncertain model parameter that is statistically conditioned to observations through a sequential ensemble based estimator to produce inverse or posterior bathymetric estimates and uncertainties.

4.3.1 Mathematical statement of the inverse problem

Up to this point, at the beginning of each hour, observed dissipation fields and a measure of its error are given. On the other hand, numerical models able to predict wave breaking dissipation on numerical grids over known bathymetry exist. If it is assumed that the model of choice, f, provides an accurate physics representation, and that it is driven by perfect initial and boundary conditions, it is possible to assume that its errors stem only from uncertain bathymetry. Thus, input bathymetry can be written as,

$$h^f = h^t + p, \tag{4.10}$$

where h^t is the true bathymetric field and p is an aditive error. When this is passed as input, the model outcome may deviate from the true dissipation field, D^t, as it contains errors, q,

$$f(h^t + p) = D^t + q. \tag{4.11}$$

The aim now is to infer bathymetry based on this knowledge, that is, obtain an optimal estimate of the true state on the model grid, $f(h^t) = D^t$, given the observations, that are themselves subjected to errors,

$$d = D^{obs} = L(D^t) + \epsilon, \tag{4.12}$$

where L is a linear operator that maps from the numerical grid to the observational space.

To solve this ill-posed problem, the optimal estimate of the true state, ψ^a, is defined as the one that minimizes the following penalty function (e.g. *Evensen* (1994b)),

$$J[\psi] = (\psi - \psi^f)^T (C^f_{\psi\psi})^{-1} (\psi - \psi^f) + (d - M\psi)^T (C_{\epsilon\epsilon})^{-1} (d - M\psi). \tag{4.13}$$

Here $\psi = [h^T, D^T]^T$ is the state vector, which is a concatenation of all model variables at all grid points, ψ^f is a background system state from a previous model forward run or available knowledge and $C^f_{\psi\psi}$ is its covariance matrix. Similarly, d is the vector of observations, $C_{\epsilon\epsilon}$ its error covariance matrix, and $M = [0, L]$ serves to recover D from ψ.

J measures, in a weighted sense, the distance between ψ and both the model predicted solution and the current observations, and ψ^a is expected to minimize the additive errors in equations 4.10, 4.11, 4.12. It is desired that the optimal solution does not deviate far from the background solution as it contains all the model physics, and at the same time, it should be close to observations. Accordingly, inverse covariance matrices pull the solution to each side, as they are a measure of uncertainty.

In the case of Gaussian error statistics ψ^a is the maximum likelihood solution. However, as the numerical model used herein is nonlinear, statistics are likely not Gaussian. Thus, the idea of optimality is dropped, and ψ^a is said to be the least-squares or variance minimizing solution of the inverse problem.

Rigorous minimization of the penalty function 4.13 yields the following formulae for the analized state (e.g. *Evensen* (2009)),

$$\psi^a = \psi^f + K(d - M\psi^f), \tag{4.14}$$

$$C^a_{\psi\psi} = (I - KM)C^f_{\psi\psi}, \tag{4.15}$$

$$K = C^f_{\psi\psi}M^T(MC^f_{\psi\psi}M^T + C_{\epsilon\epsilon})^{-1}. \tag{4.16}$$

The set 4.14, 4.15, 4.16 can be seen as a general solution, thus the problem is reduced to a proper specification of the model covariance matrix $C^f_{\psi\psi}$, which dictates the influence of observed data on the system state. In the following, the adopted approach is explained.

4.3.2 Ensemble Kalman Filter solution

If a model forecast, ψ^f, and its error covariance, $C^f_{\psi\psi}$, are known at time t_i, when measurements, d, with error covariance $C_{\epsilon\epsilon}$ are also available, solving the system 4.14, 4.15, 4.16, provides an updated state with its analyzed error covariance, $C^a_{\psi\psi}$. As mentioned, a fundamental aspect is how to estimate the error covariance for the model forecast at time t_i. The EnKF is an assimilation technique with a formal statistical background that allows estimation of $C^f_{\psi\psi}$ and its forward propagation in time.

The essential feature of ensemble-based methods is that $C^f_{\psi\psi}$ is approximated by the sample covariance of a representative ensemble. Formally speaking, the EnKF uses the ensemble to represent the probability distribution of the system state, $pdf(\psi)$, and a Markov Chain Monte Carlo method to propagate $pdf(\psi)$ forward in time, by integrating each ensemble member as stated by the model dynamics. Further, every time new observations are available they are sequentially assimilated solving a Bayesian problem (*van Leeuwen and Evensen* (1996)). The analysis scheme is then as follows.

Suppose an ensemble of N model predictions, $\{\psi^f_1, ..., \psi^f_N\}_{t_i}$, is given at time t_i, thus computed with information from a background state at t_{i-1}. To condition the prediction to current observations, $d = D^{obs}_{t_i}$, each ensemble member has to be updated according to,

$$\psi^a_j = \psi^f_j + C^{f,e}_{\psi\psi}M^T(MC^{f,e}_{\psi\psi}M^T + C^e_{\epsilon\epsilon})^{\dagger}(d_j - M\psi^f_j), \quad \text{for} \quad j = 1, ..., N. \tag{4.17}$$

Here the superscript e is added to the covariance matrices to indicate that they are now drawn from ensembles, and $d_j = d + \epsilon_j$ denotes the j member of an ensemble of observations with mean equal to the first guess observation and covariance $C^e_{\epsilon\epsilon}$. As was shown by *Burgers et al.* (1998), it is imperative to treat observations as random variables to get an updated ensemble with the correct statistics. For the present data set, the proposed perturbation of measurements is explained in section 4.3.5. Also, † indicates a Moore-Penrose pseudo inversion to account for conditioning problems when the number of measurements is larger than the ensemble size, i.e., sample covariances are not full rank matrices (*Evensen* (2004)).

Application of 4.17 produces an analyzed ensemble, $\{\psi^a_1, ..., \psi^a_N\}_{t_i}$, whose mean and sample covariance are the variance minimizing solution and its error estimate, respectively. The inversed bathymetry is then taken from the corresponding rows of $\bar{\psi^a}$, and the updated ensemble can be integrated forward in time until new measurements are available. As a result several sequential analysis steps should retrieve improved bathymetric estimates.

Obviously, in comparison with the general solution, this scheme is an approximation whose accuracy depends on the ensemble size. Note the collapse of 4.17 to equations 4.14,4.15,4.16, when the ensemble average is taken and the ensemble size goes to infinity. In fact, when $N \to \infty$, and model dynamics are linear, the EnKF converges to the standard Kalman Filter (*Kalman* (1960)). As such, for nonlinear models $\bar{\psi^a}$ and $C^a_{\psi\psi}$ will, in general, not characterize the full-time evolution

of $pdf(\psi)$ if it is non-Gaussian. However, they determine a mean path and the dispersion arround it. Furthermore, in the field of bathymetry inversion, the work of *Wilson et al.* (2014) has proved its efficacy with excellent results.

4.3.3 Background ensemble

In the preceding sections, it has become clear that this bathymetry inversion method relies both on measurements and a set of model forecasts, which is denominated the background state. Now, insight is given about system initialization, i.e., how to create the ensemble for the first analysis step.

For this type of application, it is clarifying to disaggregate the background covariance of the model by each of the state variables in ψ,

$$C_{\psi\psi}^{f,e} = \begin{pmatrix} C_{hh}^{f,e} & C_{hD}^{f,e} \\ C_{Dh}^{f,e} & C_{DD}^{f,e} \end{pmatrix}. \tag{4.18}$$

As dissipation is computed by the model, it is then clear from 4.18 that initialization hangs on the specification of the prior bathymetric covariance matrix, $C_{hh}^{f,e}$. For the first assimilation cycle, this is done adding proper perturbations to an initial bathymetry in the following way.

Pseudo-random fields with zero mean are generated with the Fourier Transform method described in the appendix of *Evensen* (1994a), which draws from the gaussian covariance,

$$C_{hh}(\Delta x, \Delta y) = \sigma_z^2 \exp\left[-\left(\frac{\Delta x^2}{L_x^2} + \frac{\Delta y^2}{L_y^2}\right)\right], \tag{4.19}$$

where L_x, L_y and σ_z are user-specified horizontal and vertical length scales, that influence the smoothness and amplitude of the generated fields, and $\Delta x, \Delta y$ are the distances between points in the numerical grid. For completeness, a brief outline of *Evensen* (1994a) method is given in appendix A.

Then, the random perturbations are added to an initial background bathymetry, which is selected from available knowledge. In this case, a two-portion model for beach profiles in equilibrium from *Inman et al.* (1993) is used, which fits two classic Dean-Brunn profiles, one for the shoaling zone and the other for the bar-berm portion. Calibration of the profiles was done iteratively until a reasonable match was found in the shorerise portion and the upper beach face against in situ data. However, this particular initial profile is not a requisite for the present inversion procedure. In fact, better estimates should benefit the overall system performance. Here, given the lack of further morphological information, the equilibrium beach profile is used as a fair depth interpolation between the offshore and shoreline boundaries.

Finally, it bears noting that after the first assimilation step the ensemble evolves via data assimilation alone, and no further random bathymetric field generation is needed.

4.3.4 Forward model

The numerical model used to predict roller dissipation consists of independent wave and roller modules. *SWAN* (*Booij et al.* (1999)) is used to simulate incident waves, whose wave spectral predictions are used to solve the roller energy conservation equation.

The model domain extends from the shoreline ($5cm$ depth contour) to $x = 900m$, and from $y = 380m$ to $y = 1150$, with grid spacing of $10m$ in both directions. Periodic boundary conditions are used in the alongshore direction, and the regions defined by $y > 1000m$ and $y < 530m$ are used as artificial buffer zones where bathymetry is smoothly ramped to satisfy periodicity. Also, buffer zones are discarded in the assimilation steps and reapplied every time bathymetry is updated.

The wave part of the model solves the stationary conservation of wave action (*Holthuijsen* (2007)), which governs the transformation of wave energy from the offshore boundary to the shoreline. The only source/sink term for wave energy is wave breaking dissipation D_{br}, which is included in *SWAN* by means of *Battjes and Janssen* (1978) parametrization with default parameters.

At each model time, measured spectra from the 8m-Array are used as stationay offshore boundary conditions, which are assumed alongshore uniform. When model times are not centered on the $3h$ analysis windows of data (section 4.1.1), spectra are time interpolated using the *SWAN* internal routine (outline available in *Swan scientific and technical documentation*, at swanmodel.sourceforge.net/). Also, tidal elevations are included as spatially constant offsets in the mean water level for each model run. This means that the inversion technique estimates bathymetry with respect to a constant vertical datum, rather than computing water depth at each assimilation cycle.

Next, *SWAN* outputs are passed to a roller evolution model that solves for the roller dissipation. Following *Reniers et al.* (2004) the roller energy conservation equation reads,

$$\frac{\partial}{\partial x}(2E_r c\cos(\alpha)) + \frac{\partial}{\partial y}(2E_r c\sin(\alpha)) = -D_r + D_{br}, \tag{4.20}$$

where E_r is the roller energy, c is the along ray celerity and α the wave direction. Furthermore, the roller dissipation can be expressed in terms of E_r as (*Svendsen* (1984); *Deigaard* (1993); *Duncan* (1981)),

$$D_r = \frac{2gE_r}{c}\sin(\beta)\cos(\beta), \tag{4.21}$$

where the front slope angle is chosen to be $\beta = 6°$, based on longshore current model calibration experiments for this site and same roller formulation (*Ruessink et al.* (2001)). Equation 4.20 is solved numerically using a finite difference scheme (described in appendix B) starting at the offshore boundary, where $E_r = 0$ is imposed.

Finally, it is to be noted that bathymetry is not restricted to be positive. Indeed, negative values (i.e., above mean sea level) should be interpreted as dry land. However, negative depths are problematic at locations where dissipation is measured. In that case, it is not possible to sample from the ensemble as required by equation 4.17. To avoid this issue, the criteria used by *Wilson et al.* (2014) are adapted to this application. First, only one zero-crossing of still water depth is allowed for every alongshore location, meaning the shoreline is a single valued function of y and no "islands" are allowed. This is enforced by setting depths to a minimum value of $0.25m$ at all points offshore from the first zero-crossing, in all cross shore transects where more than one zero-crossing exists. In cases where this adjustment causes depth changes of more than 0.5m the realization is removed from the ensemble. If, after these changes, a given ensemble member still reports dry points where dissipation is observed, that realization is also removed from the ensemble.

Over time, the above rules might cause unexpected ensemble shrinkage. To avoid this, the ensemble is resampled after each assimilation step, producing a new ensemble of size N with preserved mean and covariance. This is done using the resampling script from the EnKF-Matlab package by P. Sakov (available at https://enkf.nersc.no/Code/EnKF-Matlab/). This code computes the singular value decomposition of the ensemble and replaces the right singular vectors with an $N \times N$ random matrix with orthogonal rows. The outline of this method is analogous to what is presented in the next section.

4.3.5 Perturbation of measurements

As mentioned in section 4.3.2, *Burgers et al.* (1998) showed that it is essential to treat measurements as random variables to obtain an analyzed ensemble with the correct covariance. At each observational time, this is done by adding proper perturbations, with covariance $C_{\epsilon\epsilon}$, to the first guess measurements $d = D_{t_i}^{obs}$. In the following, the adopted approach to generate random perturbations from the measurement error covariance is presented. This is based on the improved sampling scheme proposed by *Evensen* (2009).

What is looked for is a matrix $A' \in \Re^{n\times N}$, where each column contains the perturbation vectors, $\epsilon_j = d_j - d$, and n and N are the number of observations and the ensemble size respectively. If the singular value decomposition of the perturbation matrix is computed,

$$A' = U\Sigma V^T, \tag{4.22}$$

where, by definition, the left singular vectors $U \in \Re^{n \times n}$ and the singular values in $\Sigma \in \Re^{n \times N}$ are, respectively, the eigenvectors and the square root of the eigenvalues of

$$A'(A')^T = C^e_{\epsilon\epsilon}(N-1) \simeq C_{\epsilon\epsilon}(N-1), \tag{4.23}$$

then it can be noted that perturbations can be sampled from,

$$A' = U\Sigma\Theta^T, \tag{4.24}$$

where $\Theta \in \Re^{N \times N}$ is a random orthogonal matrix, if it is ensured that the first N singular vectors in U are similar to the first N eigenvectors of $C_{\epsilon\epsilon}$. Following *Evensen* (2009), application of equation 4.24 is done with the subsequent algorithm.

First, the single value decomposition of $C_{\epsilon\epsilon}(m-1)$ is computed where m is the rank of the error covariance matrix, and a start ensemble is sampled from the multiplication of its first m left singular vectors, $\hat{U} \in \Re^{n \times m}$, with the element-wise square root of the first m singular values, $\hat{\Sigma} \in \Re^{m \times m}$. Thus, a basis, $\hat{A}' \in \Re^{n \times m}$, for the vector space from which A' can be sampled is computed. Obviously, further sampling is needed to produce random but coherent perturbations.

Accordingly, the final perturbations matrix is sampled from,

$$A' = [\ \hat{U}, 0_{n \times (n-m)}]\ \ \tilde{\Sigma}\,\Theta^T, \tag{4.25}$$

where in contrast to equation 4.24, $\tilde{\Sigma} \in \Re^{n \times b}$ is a spectrum that includes more than the first N singular values ($N \leq b \leq m$) to avoid too smooth realizations, and that also penalizes high wave numbers. In coding notation,

$$\tilde{\Sigma}(:,:) = \sqrt{\frac{b}{m}}\left[\hat{\Sigma}(:, 1:b); 0_{(n-m)\times b}\right], \tag{4.26}$$

and $\Theta \in \Re^{N \times b}$ is a random matrix with orthonormal rows. Thus, each row in Θ defines a random convex linear combination that results in a random realization in the vector space defined by $C_{\epsilon\epsilon}$. For the present data set, and for automatization purposes b is defined as the minimum between m and 1.5 times the ensemble size.

Finally, to ensure that the perturbations average is zero and that their variance is as specified, the sample mean is subtracted and ensemble members are rescaled.

4.3.6 Known shortcomings

Ensemble-based inversion methods have two known intrinsic shortcomings that provoke filter divergence, which is defined as the situation when the ensemble spread gets too low and the system rejects information from measurements. Fortunately, ad hoc but simple ways to overcome these issues have been studied and have been accepted as required by the data assimilation community. In the following, both are briefly explained and the implementation of its solution is presented.

Covariance localization

The use of a finite ensemble introduces sampling errors in the model covariance matrix, which manifest as spurious long-range correlations between state variables expected to be uncorrelated. Thus, during the analysis step variables away from the observations might be updated unphysically. After many assimilation cycles spurious updates may cancel out, but at every step, there is a reduction of ensemble variance that underestimates true variance (*Evensen* (2009)).

In this application, to control long-range spurious correlations the covariance localization approach is followed. Model covariance matrices are localized with a Schur product with a correlation function with local support (*Houtekamer and Mitchell* (2001); *Hamill et al.* (2001)). That is, $C^{f,e}_{\psi\psi}$ is element-wise multiplied with a correlation matrix that effectively sets to zero correlations between points separated by more than a user-specified distance.

A fifth-order piece-wise rational function from *Gaspari and Cohn* (1999) is used, which reads,

$$\Omega(z,l_c)=\begin{cases}-\frac{1}{4}(\frac{z}{l_c})^5+\frac{1}{2}(\frac{z}{l_c})^4+\frac{5}{8}(\frac{z}{l_c})^3-\frac{5}{3}(\frac{z}{l_c})^2, & 0\leq z\leq l_c\\ \frac{1}{12}(\frac{z}{l_c})^5-\frac{1}{2}(\frac{z}{l_c})^4+\frac{5}{8}(\frac{z}{l_c})^3+\frac{5}{3}(\frac{z}{l_c})^2-5(\frac{z}{l_c})+4-\frac{2}{3}(\frac{z}{l_c})^{-1}, & l_c<z\leq 2l_c\\ 0, & z>2l_c\end{cases} \tag{4.27}$$

Here z is the distance between a pair of grid points, and l_c the user-specified localization radii or lenght scale. Ω has a Gaussian shape, except that it decreases to zero at the finite distance $2l_c$.

Covariance localization introduces the following minor change in the analysis equation 4.17,

$$C^{f,e}_{\psi\psi}\leftarrow\rho\circ C^{f,e}_{\psi\psi}, \tag{4.28}$$

where ρ is the matrix arrengement of Ω and $\circ$ denotes the Schur product. The Schur product theorem (*Horn and Johnson* (2012)) states that the upgraded model error covariance matrix 4.28 is positive semidefinite, thus a proper covariance matrix.

Inflation

Inflation is the procedure by which the analyzed ensemble variance is artificially increased before the next update step. This is needed because as observations are assimilated the ensemble variance is reduced due to its finite size. And in this particular application, it can be interpreted as a variance growth accounting for not modeled sediment transport that may cause bathymetric changes unseen by the inversion technique.

Several approaches to inflate the model covariance have been developed (see *Carrassi et al.* (2018) for a recent review). Here, an additive approach is followed with the process error from *Holman et al.* (2013). This approach proved to be useful in *Wilson et al.* (2014) application of the EnKF for bathymetry inversion due to its ease of implementation and interpretation.

The background bathymetry ensemble, $h^f_{t_{i+1}}$, for assimilation step t_{i+1} is obtained from,

$$h^f_{t_{i+1},j}=h^a_{t_i,j}+\sqrt{Q'}\delta h_j\quad\text{for}\quad j=1,...,N. \tag{4.29}$$

This is, each j member of the analyzed ensemble from the previous time step, $h^a_{t_i,j}$, is augmented by adding the random perturbations $\sqrt{Q'}\delta h_j$ to it. Here, δh is a random ensemble with unit variance created with the procedure from section 4.3.3 with the same length scales, and Q' a spatially variable variance envelope.

The definition of Q' is based on the empirical process error Q, that *Holman et al.* (2013) derived with 36 almost daily CRAB surveys during the Sandy-Duck experiment (from 22 Sept. to 30 Oct. 1997 at the FRF). By comparing, from consecutive surveys, the alongshore-mean-squared cross-shore bottom deviations with offshore significant wave height, they fitted the following equation,

$$Q(x,H_{m0})=C_Q H^2_{m0}\exp\left[-\frac{(x-x_0)^2}{\sigma_x^2}\right]\Delta t, \tag{4.30}$$

where x is the cross-shore coordinate, H_{m0} the offshore measured significant wave height, $C_Q=0.067/day$ a fitting parameter, and $x_0=150m$ with $\sigma_x=100m$ reflect typical wave breaking location at this beach. Lastly, Δt is the time interval between survyes in days. For the present purposes, Δt is set to 1 hour, the time interval between the arrival of remote sensing data, and H_{m0} is interpolated from the 8m-Array measurements. However, care should be taken when modeling process errors with equation 4.30 at other sites, and when the time interval between observations is longer than a day. Perhaps, in the latter situation an evolutive model for the process error, like the one proposed by *van Dongeren et al.* (2008), is more attractive as it tapers Q with a *tanh* term over time.

Finally, thresholds are applied to Q to keep the background ensemble standard deviation between the user-defined bounds σ_{min} and σ_{max},

$$Q'(x,y)=\begin{cases}\sigma^2_{min}-(\sigma^a_{h,t_i})^2, & Q+(\sigma^a_{h,t_i})^2<\sigma^2_{min}\\ Q, & \sigma^2_{min}\leq Q+(\sigma^a_{h,t_i})^2\leq\sigma^2_{max}\\ \sigma^2_{max}-(\sigma^a_{h,t_i})^2, & Q+(\sigma^a_{h,t_i})^2>\sigma^2_{max}\end{cases} \tag{4.31}$$

where $(\sigma^a_{h,t_i})^2$ is the variance of the analyzed bathymetry ensemble at t_i. Following the recomentadion of *Wilson et al.* (2014), the bounds are set as $\sigma_{min} = 0.25m$ and $\sigma_{max} = 0.75m$. The lower threshold is set equal to the minimum expected error of the bathymetry inversion prediction, thus directly preventing filter divergence. On the other hand, σ_{max} avoids unbounded variance growth in sparsely observed regions, i.e., outside the surf zone. For the present purposes, Q' effectively controls the ensemble variance at locations where it is heavily reduced due to the impact of observations.

Chapter 5

Results

In the following, the results from the methodology described in the previous chapter are presented. In the first section, an example of the remotely sensed wave breaking dissipation fields is shown, including an examination of its error estimates. Secondly, the results of a bathymetry inversion experiment are presented and analyzed.

5.1 Observational data example

5.1.1 Qualitative validation

Figure 5.1(a) shows an example of the remotely sensed roller dissipation fields for a pair of video and radar data recorded at 14:59, Sep. 10th. This observational time was arbitrarily selected as it registers the lowest tidal elevation for the present data set (see figure 5.4), thus more wave breaking over the bar. On the other side, panel (b) shows the roller dissipation as predicted by the forward model over the measured bathymetry from the 6th of Sep. LARC survey, along with

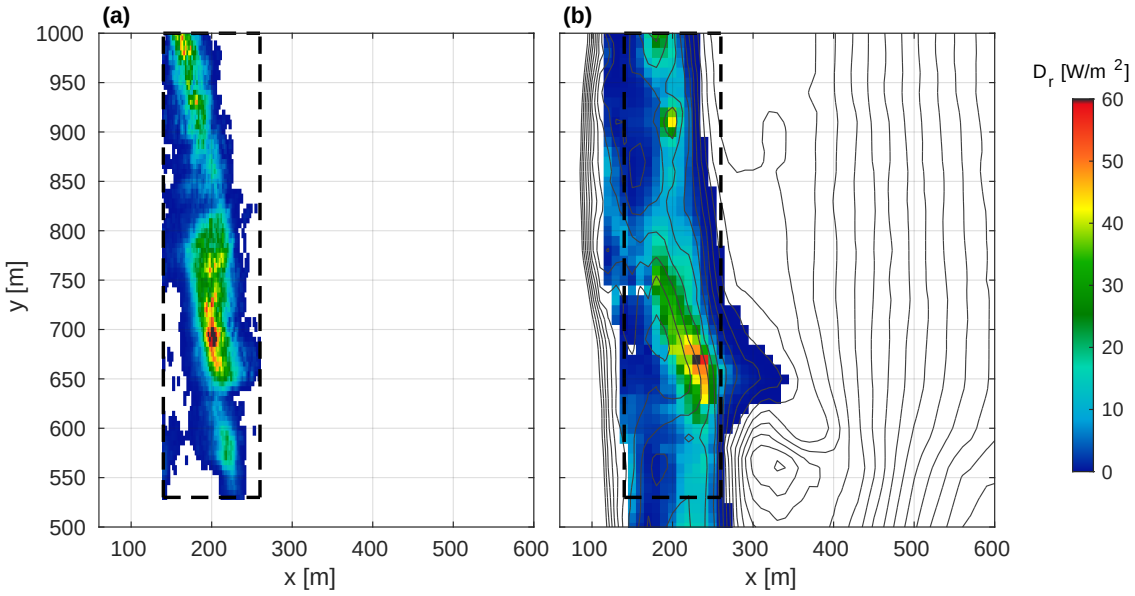

Figure 5.1: Qualitative validation. Roller dissipation at 14:59, 10th Sep. 2010. From remote sensing (a) and predicted by the forward model (b), over measured bathymetry from the 6th Sep. LARC survey (gray contour lines every $0.25m$, starting at $h = 0m$). Black dashed lines mark the remote sensing domain in both plots.

the corresponding wave forcing and tidal elevation for the target time. Further, the remotely sensed roller dissipation was computed with $\theta = 24°$, which at this point might be considered as a rudimentary calibration parameter.

In light of the similarity between both results, *Díaz et al.* (2017) considered their algorithms as valid. Here, figure 5.1 also demonstrates that the forward model could agree well with remote sensing data, given accurate bathymetry. In this case the model correctly predicts wave breaking dissipation over the offshore sandbar and smaler dissipation in the rip channel region, approximately at $800 < y < 950$ (*Haller et al.* (2014)). Also, figure 5.1(b) highlights the sensitivity of the model output to bathymetry, specifically to the sandbar located around $x \approx 200m$. This shows the roller dissipation depth dependence that is exploited in this work. The model does not predict the shore break dissipation due to the forward stepping nature of the numerical scheme used to solve equation 4.20. This is not an issue for the inversion algorithm as it assimilates outer bar roller dissipation, which is the actual area of interest.

5.1.2 Observational errors

As stated in the previous chapter, it is assumed that all model errors are caused solely by errors in bathymetry and that this is accounted for with an ensemble representation initially drawn from a Gaussian covariance, hence, with known statistics. Similarly, measurement errors are modeled with an ensemble representation too, but in this case drawn from a covariance matrix given by a heuristic approach dependent on data (section 4.2.3). In the following, the measurement perturbations produced by the method described in section 4.3.5 are shown.

Figure 5.2(a) exhibits the sample standard deviation of the measurement ensemble, i.e., the square root of the diagonal terms of the observational error covariance matrix (equation 4.9), for the same observational time as figure 5.1. As expected, the observational errors follow the spatial distribution of the measured roller dissipation D_r. This is due to the threshold variation scheme, that changes the measured roller lengths where they are detected. If the threshold variation method gives rise to small or null changes in dissipation, the standard deviation is set as the hardcoded lower bound (10% of the highest observation, $7.3W/m^2$ for this example).

Figure 5.2(b) shows the measurement perturbations for the sample points marked with black

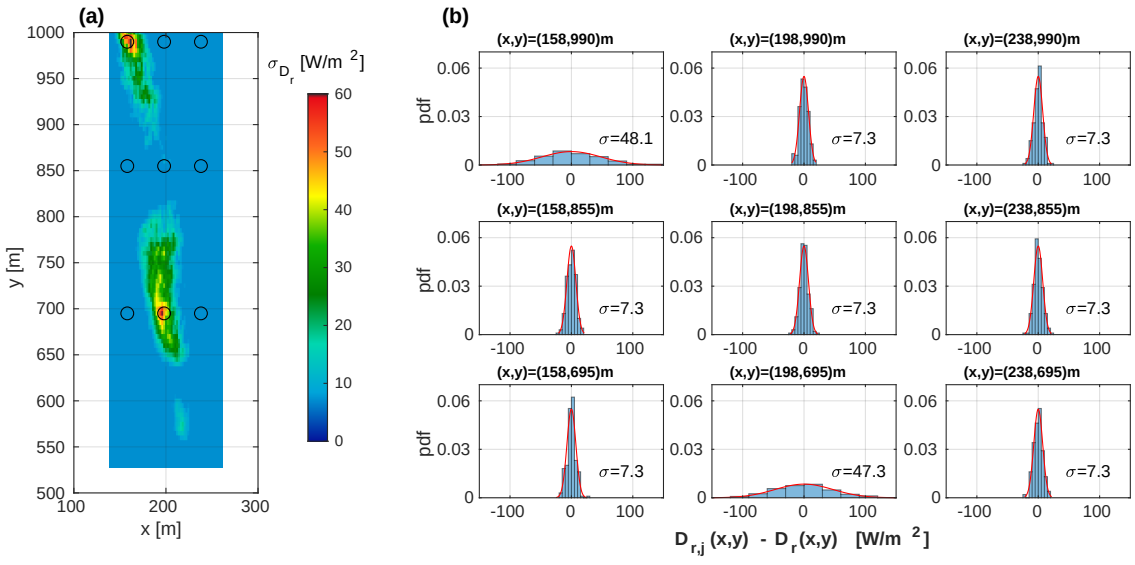

Figure 5.2: Measurement errors. Standard deviation of remotely sensed roller dissipation (a). In (b) the normalized histograms of the measurement perturbations (blue bars), and fitted Gaussian distributions (red lines) are shown for the sample points marked with black circles in panel (a). The standard deviation (σ in W/m^2) of the fitted distributions are shown in each subplot.

circles in (a). First, it should be noted that modeled perturbations show an almost symmetric distribution around the ensemble mean. This result suggests that an eventual abuse in equation 4.9 is discarded. Recall that the sample covariance in equation 4.9 is calculated from an ensemble of dissipation fields drawn from threshold variations. Specifically, what is meant here, is that the sample mean internally used in equation 4.9 is not necessarily equal to the dissipation field computed with the optimal thresholds, due to the likely nonlinear nature of the detection algorithm. Also, figure 5.2 clearly reflects the sensitivity of *Díaz et al.* (2017) procedure to threshold selection, as the histograms are flatter at points where measured dissipation is significantly greater than zero (cf. figure 5.1(a)).

Secondly, it is interesting to note the ability of the measurement perturbation algorithm to simulate the correct error statistics. All shown perturbations in figure 5.2(b) have zero mean and the corresponding standard deviation, as expected from panel (a). Nonlocal error statistics also behave as expected (these are not shown here, but their influence will be tested in the following chapter). In addition, the simulated error statistics behave Gaussian-like, as can be seen by their close match to the fitted Gaussian distributions (red lines in each subplot). This was not intended in the first place, but it is because the covariance is a first-order moment. So sampled errors are Gaussian random variables by construction, even if the original dataset was not. Due to the lack of further knowledge regarding the statistics of the detection algorithm, the measurement perturbation algorithm is considered appropriate for the present purposes, as the EnKF analysis equations also disregard higher-order moments.

Finally, it is worth mentioning that the simulated observational perturbations result in some ensemble members showing patches of negative roller dissipation. This comes from the built-in assumption that D_r is a Gaussian random variable, which is obviously untrue, as negative dissipation is impossible. While this non-physical situation might result in suboptimal EnKF results and improvements such as anamorphosis transforms (e.g. *Simon and Bertino* (2009); *Bocquet et al.* (2010)) or more sophisticated filters could be applied (e.g. *Bishop* (2016); *Beal et al.* (2010)), here it is not considered a major issue for the inversion system, mainly because of the EnKF analysis steps linearity. In other words, inversion results are the same when the analysis equation is applied to each ensemble member and the average is taken, and when the average of equation 4.17 is taken first and the analysis is performed only for the mean (thus removing bathymetry and measurement perturbations, i.e., negative dissipation rates). Consequently, it is hypothesized (but not proven) that the filter suboptimality affects to a lesser extent the ensemble mean, and somehow stronger

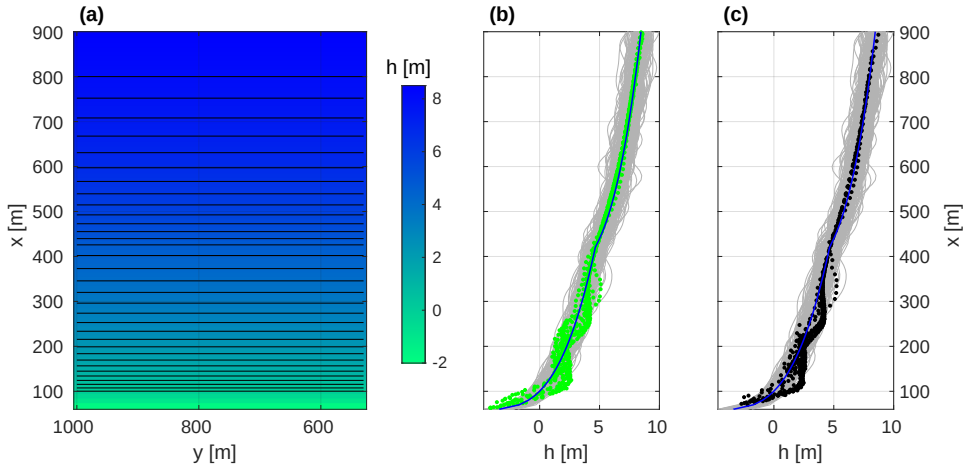

Figure 5.3: Initial bathymetry. Alongshore uniform initially presumed bathymetry (a) (solid lines indicate contours every $0.25m$, starting at $h = 0m$). The profile is compared to the measured LARC surveys (to the north of the FRF pier) from 6 Sep. (b) and 15 Sep. (c) illustrated with green and black points, respectively. In (b) and (c) the thin blue lines are the initial profile and light grey lines are the initial perturbations along the central cross-shore transect.

the ensemble spread, i.e., the uncertainty of the result, which has also been reported as troubling in other inversion algorithms (*Brodie et al.* (2018)). Anyhow, future applications or research regarding this methodology could benefit from the mentioned workarounds. In other words, this means assuming a more accurate distribution for the observations, i.e., applying a transformation to the data, chosen to create an observable that is closer to a Gaussian distribution.

5.2 Bathymetry inversion experiment

In this section, the results of a specific inversion experiment, i.e., with a fixed set of parameters, are presented in detail. At the end of this section, a detailed analysis of the results is given. In light of the results, the analysis is intended for understanding the specific strengths and limitations of this bathymetry inversion approach, before dealing with general discussions in chapter 6.

5.2.1 Experimental setup

Initialization

This, and all cases presented below, are initialized with bathymetric ensembles whose mean is shown in figure 5.3(a). It should be noted that this alongshore uniform profile contains very little information about the true morphological state of the beach. As illustrated in figure 5.3(b) and (c) it only matches measured depths for $x > 400m$ (presumably, the closure depth as can be seen

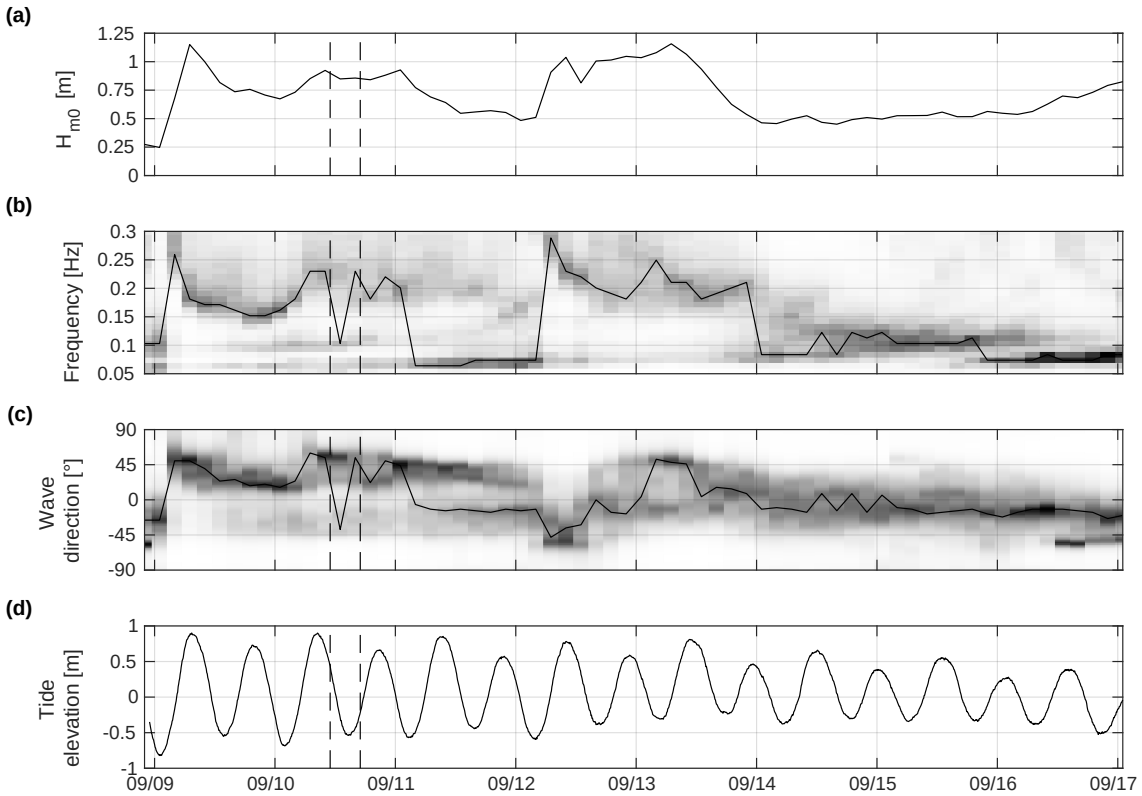

Figure 5.4: Wave conditions observed in $8m$ depth during the experiment versus time in EST. The start and end times of the data assimilation experiments of section 5.2 are marked with dashed vertical lines. Significant wave height (a), integrated frequency and directional wave spectrum respectively in (b) and (c) (normalized to unit energy for each time), with peak frequency and direction marked with black lines. Wave direction is measured counterclockwise from the positive x-axis to the direction waves come from. Observed tidal elevations (d).

in the scatter of measured depths) and the position of the shoreline, roughly at $x = 100m$. But most notably, the surf zone presumed bathymetry does not include any of the actual features, nor the variability seen during the experiment (cf. figure 5.5(c),(d)).

Uncertainty for the background bathymetry, C_{hh}, was initialized with the method described in section 4.3.3 with length scales $L_x = L_y = 100/\sqrt{3}m$ and $\sigma_z = 0.5m$ for a $N = 200$ ensemble size. The initial perturbations along an arbitrarily selected cross-shore transect are shown in light grey in figure 5.3 (b) and (c). Its length scales are in agreement with the ones used by *Wilson et al.* (2014). They argued that the across-shore length scale is consistent with values estimated from the sample covariance of 253 historical surveys, for the bar region, i.e., $100 < x < 400m$, and on the other hand, that the alongshore correlations are more complex and not well modeled with a Gaussian covariance. However, as they mention, such alongshore covariance information would, in general, not be known a priori. Thus, an isotropic covariance is used instead. This guarantees that corrections to bathymetry are due to assimilated data rather than user-specified prior knowledge.

Environmental conditions

Conditions observed during the experiment are shown in figure 5.4. Two wave events exceeding $0.75m$ significant wave height were observed, during which wave frequencies were around $5s$ with a wide range of incidence angles.

The inversion system will be tested using a $6h$ period of data during daylight hours ($1000-1600$ EST) on 10 September, during the first wave event. This time window is marked with vertical lines in figure 5.4. In the course of this time interval, the significant wave height was around $0.85m$, and wave spectra consisted of northerly short wind waves and swell waves approaching from the south. The observed dynamics were spatially nonuniform, mostly due to nonuniform bathymetric features. Noticeably, a rip current was observed during low tide at $y \approx 800 - 950m$, presumably because of a gap in the nearshore sandbar/terrace system (*Wilson et al.* (2014); *Haller et al.* (2014)).

Data assimilation setup

The methodology for bathymetry inversion presented in the previous chapter hangs on some tunable parameters, namely: the roller front slope angle θ, and the localization range used for the observational and model error covariance matrices, respectively l_c^{obs} and l_c^f.

The roller inclination controls its dissipation rate and is directly related to the inverted depths. For the present experiment, it has been set to $\theta = 24°$ based on the rudimentary calibration shown in figure 5.1.1 and on the sensitivity analysis of section 6.1.1. This value is also consistent with the range reported in the literature for both laboratory and field data (*Duncan* (1981); *Stive and De Vriend* (1994); *Dally and Brown* (1995); *Haller and Catalán* (2009); *Carini et al.* (2015); *Zhang et al.* (2017); *Ruessink et al.* (2001)).

The localization ranges are set to $l_c^{obs} = 37.5m$ and $l_c^f = 75m$. The former is also based on the following sensitivity analysis, and the latter is in agreement with the value used by *Wilson et al.* (2014).

5.2.2 Results

Figure 5.5(b) shows the final estimate after six assimilation cycles (panel (a) shows the initially presumed bathymetry again, for direct comparison). In situ surveys from the 6th Sep. (c) and the 15th (d) allow a qualitative evaluation of the result. The color bar at far right applies to all plots and its transparency represents uncertainty, estimated as the ensemble standard deviation (*Evensen* (2009)).

First, the ability of the system to retrieve the subaquatic orientation of the beach stands out. This is noticeable in the oblique nearshore terrace (between $1m$ and $3m$ depth contours) that was initially absent. Besides, it correctly estimates the position and amplitude of the sandbar and its interruption by a rip channel, between $y \approx 800 - 950m$, where *Haller et al.* (2014) observed a rip current during low tide.

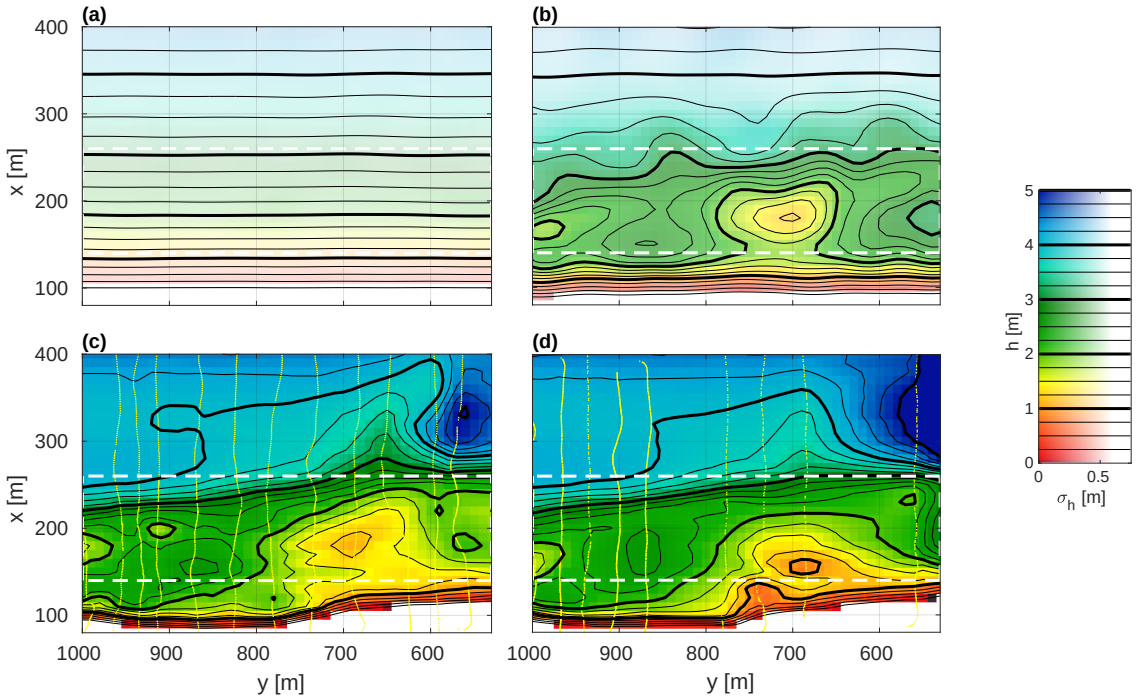

Figure 5.5: Results. Initial bathymetry (a), inverted bathymetry after 6 assimilation cycles during 10 Sep. (b), in situ measurements from 6 Sep. (c) and 15 Sep. (d). Yellow dots indicate individual surveyed points and dashed lines are the remote data boundaries. Color bar transparency indicates uncertainty of the estimates. Contour lines apply to all panels. Depths are relative to the NAVD88.

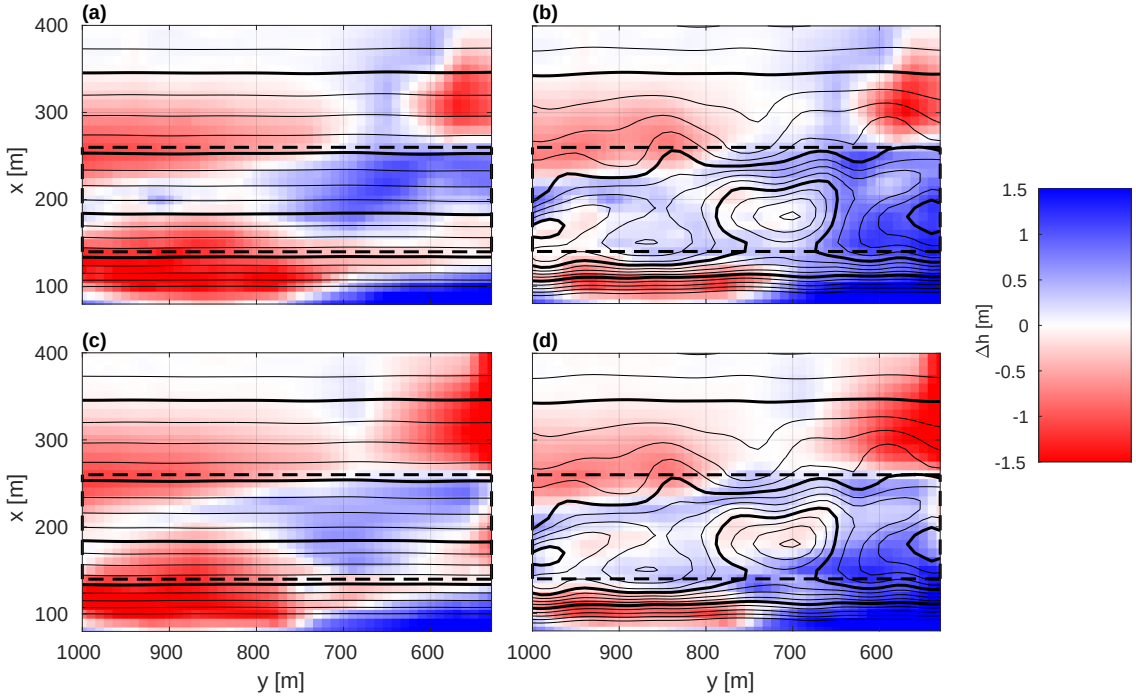

Figure 5.6: Difference between estimated bathymetry and gridded survey data. (a) and (b) use data from the 6 Sep., showing differences before and after data assimilation, respectively. (c) and (d) are the same but using data from 15 Sep. Positive differences indicate depth overestimations. Black lines are estimated depth contours as in figure 5.5. Dashed lines are remote data boundaries.

Outside the presumed surf zone, $x > 260m$, the result is less accurate and is followed by an increase in uncertainty. Results are not as satisfactory for $y < 650m$, where the FRF pier pilings induce scour (a persistent feature at this site). Specifically, near $(x, y) \approx (150, 530)m$ the system retrieves an apparently spurious deep zone. The hole at $(x, y) \approx (170, 570)m$ in figure 5.5(c) is not real. It is an artifact of interpolation, that in the case of 6 Sept. data, is corrupted due to the lack of surveyed transects under the pier. Those transects were measured during 15 Sept., allowing a reasonable interpolation in panel (d).

To qualitatively visualize the data impact, figure 5.6 shows the differences between estimates and the in situ surveys. The left column compares the initial estimate against data from the 6th Sep. (upper row) and against data from the 15th Sep. (lower row). The right column shows the same but using the final estimate, i.e., after data assimilation. Accordingly, figure 5.6 should be analyzed per row and from left to right.

As the initial estimate contains little information about the true bathymetry, both of its plots show major differences across the domain. For that same reason, over- and underestimations of the true surf zone bathymetry are distributed with no coherent relation with the true morphology. The near-zero stripes (whiter pixels) are only due to local close matches between the initial estimate and

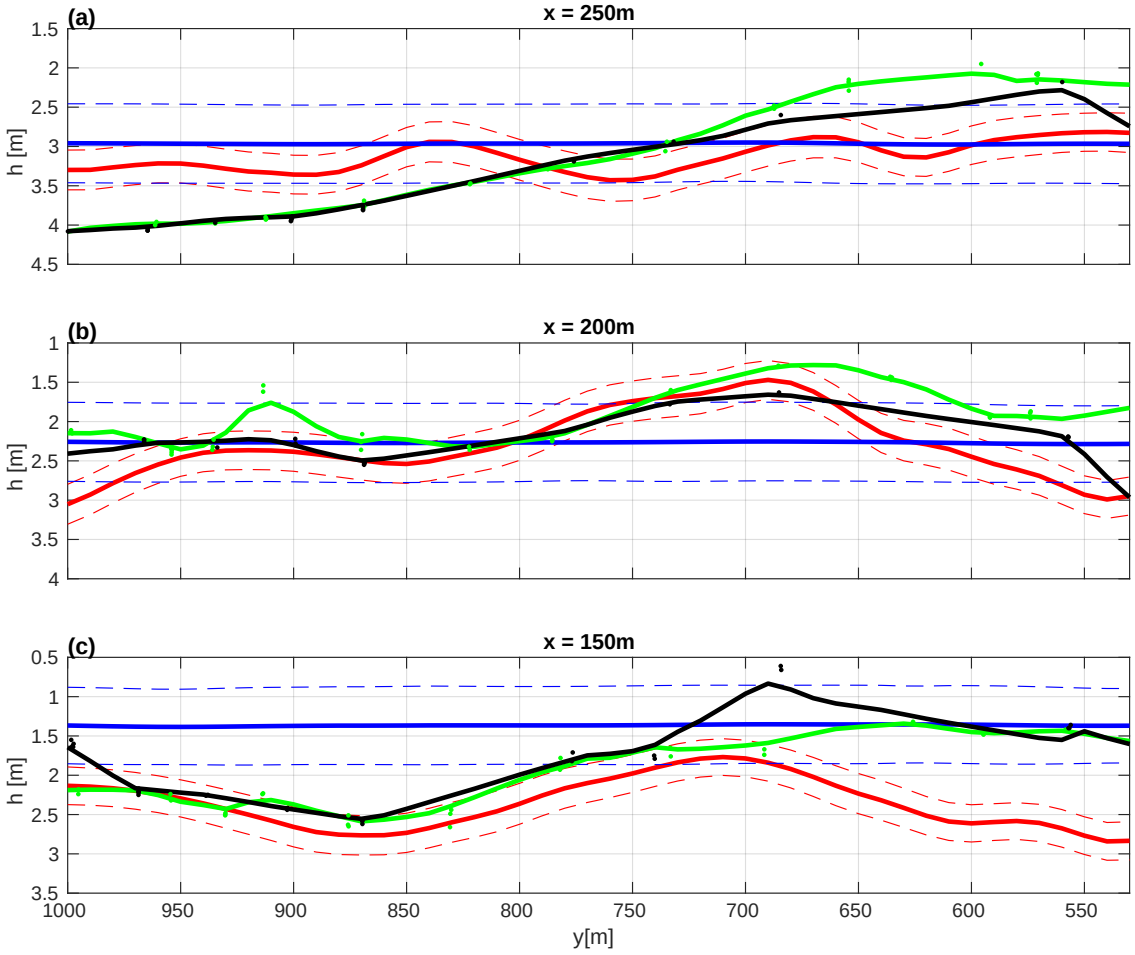

Figure 5.7: Alongshore transects at $x = 250m$ (a), $x = 200m$ (b) and $x = 150m$ (c), from initial (blue) and final (red) estimated bathymetry and $\pm$ one standard deviation (dashed lines), compared to measured bathymetry on 6 Sep. (green) and 15 Sep. (black). Dots represent measured data from within $2m$ of the alongshore transects; green and black lines are smoothed 2D interpolation of raw data, as in figure 5.5.

the surveys, and where there are clear zero crossings (from underestimations to overestimations, or vice versa).

On the other hand, the bathymetry estimate is in general improved by data impact, as can be appreciated in panels (b) and (d) of figure 5.6. In the surf zone (area bounded by black dashed lines) where $y < 650m$, depths are greatly improved after data assimilation. Specifically, differences are small over the estimated shoals located around $(x, y) \approx (150, 1000)m$ and $(x, y) \approx (200, 700)m$, and over the rip channel. These features shape a region of good skill (white oblique patches), which is in agreement with the true sandbar/terrace orientation (between the location of the mentioned shoals). As is discussed below, this region of good skill is directly related to the observed dissipation magnitude. Surrounding the region of good skill, bluish colours suggest slight depth overestimations. These are also discussed below.

In addition, offshore differences after data assimilation are not as heavily reduced. This is due to the spatially decaying influence of data, given by the relation between depth and dissipation modeled with the covariance matrix in equation 4.17 and forced by the localization function in 4.28. However, outside the surf zone, the estimated error bands are also larger (cf. figure 5.8). The result could be still considered skillful as long as the true bathymetry lies within the error bars, which is not always the case for the reasons discussed below. On the other side, near and on the landward side of the shoreline (approximately at $x \approx 100m$) interpretation of the estimated bathymetry is uncertain, as those grid points are wet only during high tide. They are thus presumably spuriously updated.

Results are further illustrated by individual alongshore and cross-shore transects. Figure 5.7 shows alongshore transects at $x = 250$, 200, and $150m$, from which it can be seen that the inversion system fairly captures the location and amplitude of the rip channel in the two shoreward transects. Similarly, the three cross-shore transects shown in figure 5.8 prove the capability of this inversion technique to retrieve good estimates of surf zone depths, as the final estimate is in good agreement with in situ data, particularly with the 6 Sep. surveyed sandbar.

There are, however, some mismatches between the final estimate and in situ data, namely: seaward and near the offshore boundary of remote data, near the FRF pier, and in the surroundings of the sandbar. They are analyzed in detail in the following section.

A final comparison is shown in figure 5.9. Regardless of which of the surveyed bathymetries should represent the true state for Sep. 10th, it can be seen in panel (a) that surf zone inverted

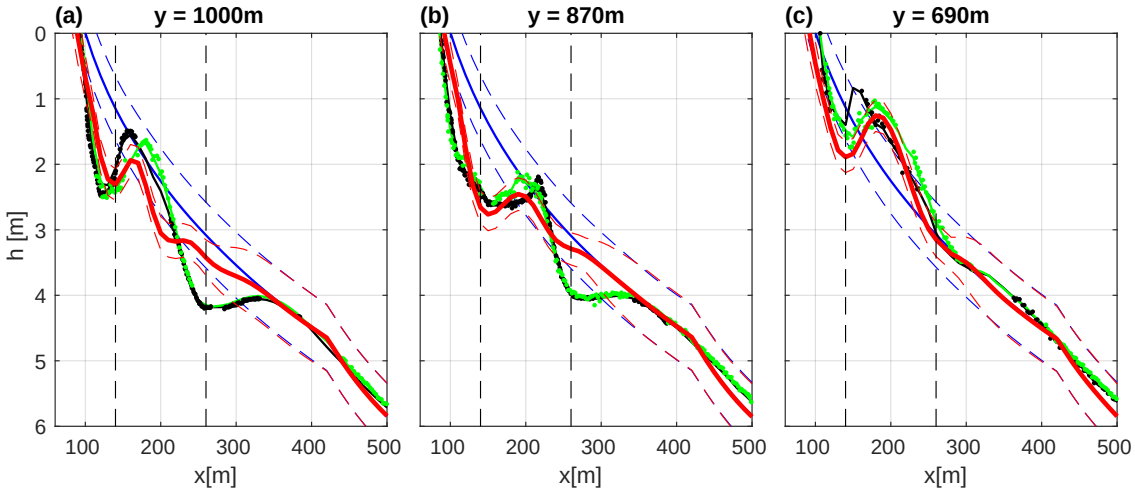

Figure 5.8: Cross-shore transects at $y = 1000m$ (a), $y = 870m$ (b) and $y = 690m$ (c), from initial (blue) and final (red) estimated bathymetry and $\pm$ one standard deviation (dashed lines), compared to measured bathymetry on 6 Sep. (green) and 15 Sep. (black). Dots represent measured data from within $5m$ of the alongshore transects; green and black lines are smoothed 2D interpolation of raw data, as in figure 5.5. Vertical dashed lines mark the observed data boundaries.

depths correlate well with both of them, mean bias is $0.11m$ and $0.08m$ deep for the 6 Sep. and 15 Sep., respectively. Also, figure 5.9(b) shows the root mean squared error evolution over time. This reflects that much of the correction is done during the first assimilation cycles, showing that for operational purposes, this approach should be able to work under rapidly changing bathymetry and that it could recover fast after periods of blackout or missed data.

Finally, comparisons with applications of the cBathy algorithm prove the efficacy of the present approach. *Honegger et al.* (2019) retrievals with X-band data gave a root-mean-squared error of $0.49m$ and $0.26m$ bias deep, in agreement with the original results of *Holman et al.* (2013) with optical data ($0.51m$ rmse and $0.19m$ bias). Final error estimates of the present approach are $0.35m$ and $10cm$ bias deep in the surf zone. Yet, a direct comparison is unfair as cBathy does not need an initial bathymetry estimate and its errors were computed over the whole domain. For that reason, figure 5.9 shows the error evolution for the whole domain and for the surf zone separately. Regardless of that, it is acknowledged that the root-mean-squared erros are of the same order, and that surf zone depth bias is considerably reduced (cf. figure 4 of *Honegger et al.* (2019)).

5.2.3 Analysis

In this section, the performance of the results is inspected in detail. The focus is on the regions of low skill mentioned above and their causes.

The first one is the prominent mismatch at the secondary terrace at $x \approx 300m$ that remains upto $x \approx 230m$ in the two northernmost cross-shore transects (figure 5.8 (a) and (b)) also visible in the $x = 250m$ alongshore transect (figure 5.7(a)). To understand this region of low skill, the roller dissipation estimates shown in figure 5.10 are analized. Panel (a) shows the dissipation estimate before the first assimilation cycle, i.e., as predicted by the forward model over the initial bathymetric ensemble, and panel (b) shows the updated dissipation after the penultimate cycle, i.e., after the assimilation of the corresponding observed dissipation, which is shown in panel (c) (white patches in figure 5.10(b) are grid points where updated dissipation is artificially negative, $O(-0.1)W/m^2$, discussed below). First, it should be noted that before assimilating any data, the forward model predicts little dissipation in the region defined approximately by $x > 230m$. Measured dissipation is also close to zero there, but specifically for $y > 850m$ it is zero over a big area (observational time 14.59 is again chosen for the same reason as in section 5.1). The close

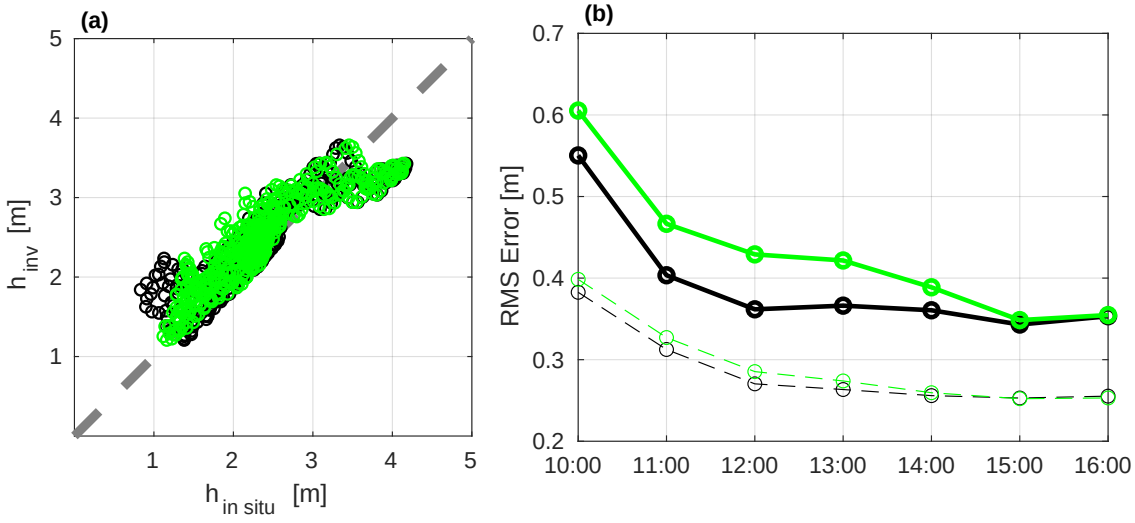

Figure 5.9: Comparison of surveyed surf zone depths ($140 < x < 260m, y > 650m$) from 6 Sep. (green) and 15 Sep. (black) to inverted depths (a). Dashed gray line denotes perfect agreement. Root mean squared deviation evolution (b) for the whole domain (dashed lines) and surf zone (solid lines), following the same color scheme.

match between predictions and observations over that area results in small innovations in equation 4.17, thus little updates. This means that the system is able to update predicted dissipation to be in agreement with observations with little impact on depth. This is what happens in figure 5.7(a) for $y > 800m$, where it can be seen that the updated bathymetry is deeper than the initial estimate but not enough to be in agreement with the surveys.

The following thought experiment is proposed to disregard the impact of the initial estimate. First, if the initial estimate were shallower, the system would have retrieved a similar final estimate, as it would have updated depths until the model predicts small or null dissipation in that region. Thus, reaching a sort of saturation, where no more deepening is needed for the forward model to predict null dissipation. Contrarily, if the initial estimate were deeper than the true depth, it is expected for the final estimate to be in agreement with in situ data at locations where observed dissipation is significantly greater than zero, thus over the sandbar, given that model predictions would already have been zero elsewhere. As this is very challenging to prove in general, an example where the initial estimate is considerably deeper is shown in appendix C.

Physically this is due to the wave breaking depth dependence, analogous to the deepwater limitation of dispersion methods discussed in chapter 2, thus dependent on wave conditions and not only on true depth. In other words, at depths greater than a certain depth (relative to the wave field conditions) waves will not break, and the roller dissipation depth dependence is off. Also, this situation is problematic for the EnKF, as it assumes that the forward model is linear, which is obviously not the case. Thus, the deepwater limitation discussed here is not only a physical constraint. This might also cause underprediction of posterior uncertainty, and is the cause of the negative dissipation rates in figure 5.10(b). As is shown in the next chapter, the hardcoded threshold for the observational errors helps balance the impact of the violation of the linearity assumption.

On a hypothetical long application of this system, it would be able to retrieve the secondary terrace under higher wave conditions, as was during run 1 of *Díaz et al.* (2017), when waves broke between $250 < x < 400m$. However, it would not necessarily reproduce the true beach recovery after such stormy conditions, as the system would again update depths on a narrower and closer to shore, surf zone.

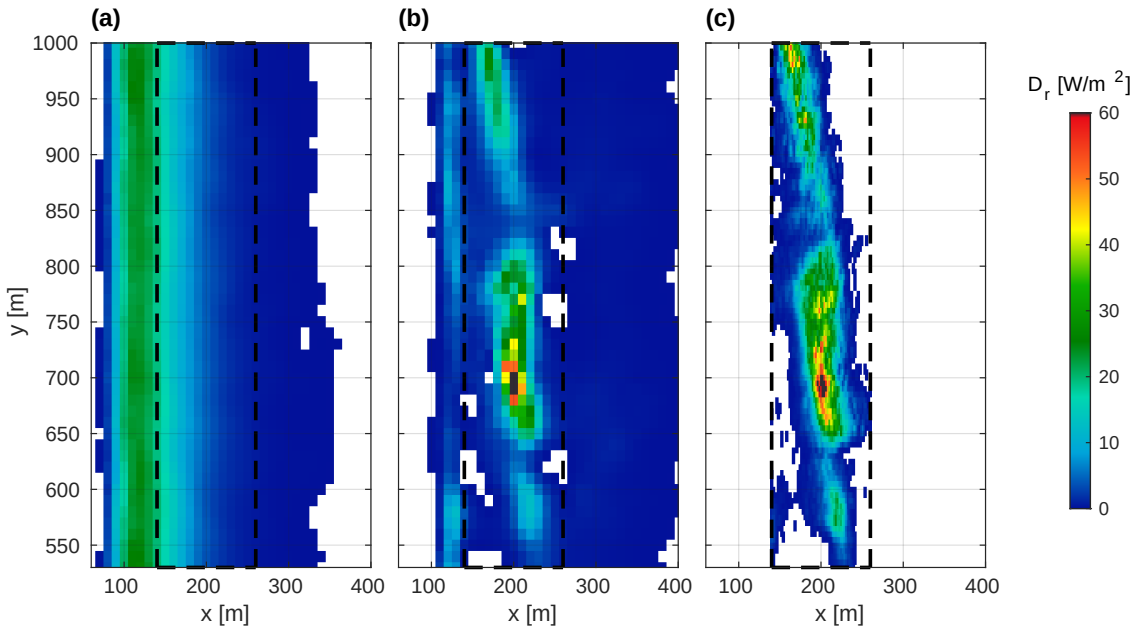

Figure 5.10: Roller dissipation estimates. Before data assimilation (a), after the penultimate assimilation cycle (b), and as estimated from remote measurements. (b) and (c) correspond to the same observational time as in figure 5.1.

The second region of low skill is evident near the FRF pier, $y < 650m$, where estimated bathymetry is systematically deeper than both surveys. This is especially apparent where observed dissipation is close to zero in the lower left-hand corner of the observational domain (figure 5.10(c)), thus retrieving a spurious deep zone. In situ data, however, do not show that feature and on the other hand, a visual inspection of optical data shows that wave breaking was infrequent there. Thus, the mismatch is presumably due to unmodeled local phenomena (possibly related to wave interactions with sharp depth gradients surrounding the pier) rather than measurement or detection errors. This issue would perhaps be reduced if the system were applied to a full tidal cycle. Unfortunately, no more data was available at the time this manuscript was prepared. In any case, this is a singularity of the field site, rather than an intrinsic deficiency of the inversion system.

The third feature of not so good skill is the slight depth overestimation surrounding the sandbar. It is noticeable, for instance, in the trough region in figure 5.7(c), where it can be seen that the final estimate gets deeper than the surveys as y decreases. Following the same local analysis as in both previous issues would lead to the same conclusion, as remotely sensed dissipation is not significantly greater than zero near its shoreward boundary during the whole time period considered. Yet, such an analysis is not appropiate in general, as dissipation has a story along wave rays (*van Dongeren et al.* (2008)). In other words, along a wave ray, energy dissipation has a spatial correlation as waves carry a finite amount of energy.

In the author's opinion, it seems surprising that inverted bathymetry is deeper in the trough, where updated dissipation is in agreement with observations (for instance for $140 < x < 180m$ and $650 < y < 800m$ in figure 5.10). This suggests that the model considers that there is still some energy to dissipate by wave breaking between the bar and the shoreline.

While this may be true, there is evidence that the depth induced wave breaking submodel used in *SWAN* might not reproduce some features well. For instance, using a large data set *Stringari and Power* (2019) proved that the fraction of broken waves as predicted by *Battjes and Janssen* (1978) formulation shows high deviations with respect to their measurements, $O(40\%)$, across natural surf zones. They attributed those deviations to the presumed wave height distributions. There are, however, other causes attributable to this formulation in *SWAN*. For example, the use of a constant breaker index ($\gamma = 0.73$), that has been suggested to produce better results when scalled with normalized wavenumbers and bottom slopes (*Ruessink et al.* (2003); *van der Westhuysen* (2010)), and the use of one-dimensional formulations in 2D setups. Particulatly, *Ruessink et al.* (2003) reported wave height overestimations in the bar trough region when using a model based on *Battjes and Janssen* (1978) formulation, suggesting underestimating of wave dissipation in the inner surf zone. While these situations could have been reduced by prior calibrations, it was decided to use *SWAN* with its default parameters, as they are still a challenge in surf zone wave spectral models. Specifically, wave breaking formulations remain heuristical and requiere further empirical and theoretical substantiation (*Salmon et al.* (2015)).

In fact, the three regions of low skill discussed above reflect a limitation of the present approach, which is that depths are not reliably updated where observed dissipation is close to zero or zero. Here they have been discussed separately to better understand present limitations, but they are all affected by the nonlinear relation between depth and roller dissipation, which is assumed as linear by the assimilation algorithm, and by the forward model wave breaking criteria. The latter appears in all surf zone wave modeling efforts and is hard to be better dealt with as long as there is no other method to directly measure dissipation or more theoretical substantiation. The former is intrinsic to this work and becomes apparent where observed dissipation is small, i.e., where the relation between h and D_r is lost. An interesting avenue in that sense would be to investigate higher-order methods to deal with nonlinearities and/or to implement a more sophisticated sampling approach, where those grid points are dealt with differently, to avoid user definitions, as the rectangular surf zone presumed here.

In summary, it is stated that the inversion approach followed in this work is able to retrieve good estimates of bathymetry where wave dynamics (or more specifically wave energy transformation) are dominated by breaking, and on the other hand, where observed dissipation is zero inverted depths are not uniquely defined.

Chapter 6

Discussion

First, different types of errors are inspected, this includes a sensitivity analysis and discussions regarding errors related to the setup of the inversion system. In a second section, some of the possibilities that arise from this work are proposed.

6.1 Error sources

6.1.1 Observational parameters

As was noted in section 5.2.1, the inversion methodology has three main tunable parameters, namely: the roller front slope angle θ, and the localization ranges for the observational and model error covariance matrices, l_c^{obs} and l_c^f respectively. The first is entirely related to the dissipation measurements, while the localization ranges are related to the data assimilation method. Here, the sensitivity of the results to θ and l_c^{obs} is analyzed, as they are intrinsic to this work, while the influence of l_c^f is left for appendix D, as it is known to affect the smoothness of the inverted batyhemtry (*Wilson et al.* (2014)).

The left column of figure 6.1 shows the impact of the roller front slope angle value while keeping all other parameters invariant, even the roller front slope angle in the forward model, $\beta = 6°$ (section 4.3.4), whose impact is also shown in appendix D with an example). As expected, higher θ values result in shallower inverted depths. This is due to the monotonic relation between the wavefront slope angle and roller dissipation, as dictated by the model 4.8. The larger the angle, the stronger dissipation is. On the other hand, in the surf zone, the forward model predicts more breaking dissipation as depth decreases, i.e., in the shoreward direction, more waves break as water gets shallower. Hence, as observed dissipation is stronger (as is in the simulations corresponding to figure 6.1(a), (c), and (e)), less depth is required in the forward model to account for the observed dissipation.

On the other side of figure 6.1, panels (b) and (d) show the impact of the localization range of the observations. These should be compared to panel (c). Although this parameter represents a distance, its influence is better understood through the observational error covariance $C_{\epsilon\epsilon}^e$. When the observational localization range is small, for instance in (b), the observational error covariance is biased toward a diagonal matrix, the ensemble spread is underestimated, and results might be overfitted to observations. On the contrary, if l_c^{obs} is large $C_{\epsilon\epsilon}^e$ is not as well-conditioned, and some bathymetric features are smeared out.

Besides, figure 6.1(f) shows the final estimate when the lower bound for the observational error is disregarded (section 4.2.3). In that case, the error estimate is zero at locations where no breaking is detected. Accordingly, the system retrieves a deeper bathymetry, as it considers observations where roller dissipation is zero to be perfect. While the last statement might be true in general, from the data assimilation perspective, and specifically for the EnKF, the use of the lower bound for observational errors balances the impact of the violation of the linearity assumption. A further case, where the lower bound was set as 20% of the maximum observed mean dissipation is presented

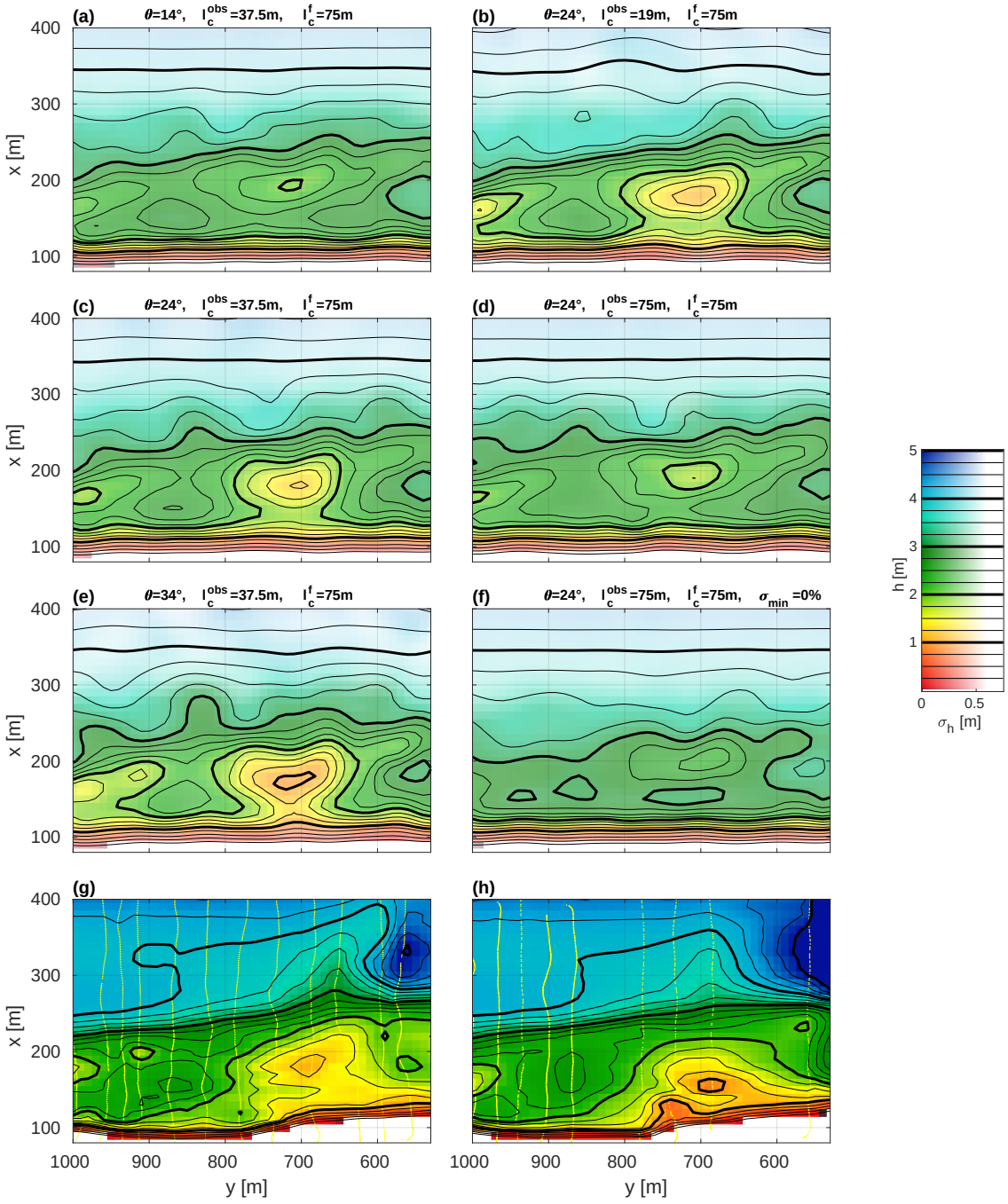

Figure 6.1: Sensitivity analysis. Panels (a - f) show the final estimates of bathymetry with the parameter values indicated in each subplot. (g) and (h) show the in situ surveys from 6 Sep. and 15 Sep. respectively.

in appendix D, where it can be seen that, when positive, this parameter has little impact.

Finally, it has to be mentioned that the values adopted for the parameters in the previous chapter were chosen in light of these analyses. Both, the roller angle and the localization range, were chosen as a balance between the extremes shown in figure 6.1. However, they have not been calibrated by any means against the surveys. Perhaps results from panel (b) might seem more attractive, but it induced a higher rate of failed members due to island generation (section 4.3.4),

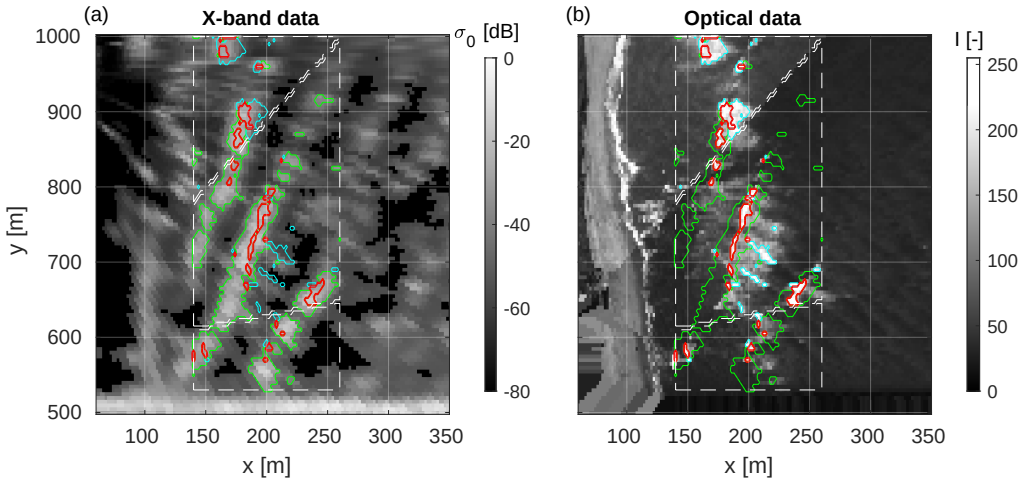

Figure 6.2: Failed breaking masks at 15:01:57, 10th Sep. 2010. Same caption as figure 4.5

whose influence in the ensemble statistics is not easily quantified. In that case, 10.6% of members were neglected and 3.4% had to be truncated to avoid that issue, in contrast to results from panel (c) where only 3.5% were discarded and 0.7% truncated. In any case, results from section 5.2.2 allowed a better understanding of the limitations of this approach.

In fact, these parameters form a space of solutions where their impacts might balance each other. In that sense, it was decided to avoid further calibrations also due to neglected uncertainties regarding other method-related causes, for instance: underreporting of breaking waves, the value of the roller mass density, and violation of the spilling breaker and roller area similarity assumptions.

In fact, the present instrumental setup might difficult the detection of some northerly wind waves. For instance, in the left panel of figure 6.2, it can be seen that the algorithm clearly detects shoaling swell waves approaching from the southeast (three high backscatter patches in diagonal roughly marked with green), and their corresponding rollers marked in red in panel (b). On the contrary, some wind waves approaching from the north, near $(x, y) = (200, 700)m$, only show high contrast in the optical band and are considered as remnant foam. A possible cause of this detection mistake is the relative position of the radar with respect to the direction of the waves. The surface normal vector at the front of the southerly waves points in the radar view direction, thus backscattering higher magnitudes than wind waves whose normal vectors point almost perpendicularly and are barely seen in the microwave data (*Catalán et al.* (2014)). This situation may have not been present in *Díaz et al.* (2017) R2 test case, where the wave spectrum was directionally narrower. Consequently, this issue was avoided with a visual inspection and manual calibration of the detection thresholds, yet it is not completely absent. Nevertheless, this is due to observational capacity and not to the algorithm proposed here.

On the other hand, the roller mass density was defined according to *Duncan* (1981), but an arbitrary increase of its value would allow lower roller angles, as both values compensate in equation 4.8. However, as it has not been measured in the surf zone, an arbitrary modification of its value would produce no objective skill improvements.

6.1.2 Error of representation and forward model setup

In this section, errors regarding the nature of observed and predicted dissipation are acknowledged. This is, the Lagrangian or Eulerian approach used in each case. First, the use of the roller module is explained. Second, the ambiguity between observations and model predictions is discussed.

The roller evolution model had to be used because *SWAN* outputs the wave breaking dissipation D_{br}, i.e., the amount of organized wave energy that is taken out from the wave field, whereas *Díaz et al.* (2017) methodology accounts for the roller dissipation D_r. Thus, it was needed to compare the correct flow quantity. In fact, the forward model predicts the roller dissipation from the wave

breaking dissipation through equation 4.20.

There is a main reason to follow this direction and not the other way around. Namely, if it were wanted to obtain D_{br} from D_r, a measure of the phase averaged velocity c would be needed. Unfortunately, neither the remote sensing algorithms used here are suitable for this purpose, nor is bathymetry known a priori to predict c with another model. Also, noisy roller dissipation measurements, as can be seen in figure 5.1(a), are likely not appropriate to be incorporated in a numerical scheme as the one used to solve equation 4.20. And at last, the rational way used to estimate the observational errors (section 4.2.3) would probably degrade if measurement perturbations were passed through a secondary model.

However, the adopted approach is acknowledged to include errors, as the phase speed was estimated, point by point, as the ratio between the mean wavelength and the peak period predicted by *SWAN*, and due to the assumption of a narrow-banded spectrum in the roller module (section 4.2.3). Yet, this was the most operational way to make comparisons between observations and model predictions.

Second, the discrepancy in the observed and predicted dissipation is perhaps the most challenging source of error to evaluate in this work. As stated in section 4.2.2, observed dissipation is a Lagrangian quantity, that is mapped onto the spatial grid by time-averaging instantaneous dissipation fields, which in turn, assume all dissipation takes place in the front of the rollers. When time-averaging over one wave period, *Díaz et al.* (2017) obtained individual wave track signatures, that were reduced when averaging over more than a hundred wave periods (as is done here).

On the other hand, the left-hand side of the wave energy equation is derived with an Eulerian approach (*Holthuijsen* (2007)), whereas the right-hand side terms are Lagrangian quantities (for instance, the *Battjes and Janssen* (1978) term) that are applied point by point even when in reality they are spatially distributed. Next, *SWAN* derived quantities are used in the roller module, that is Lagrangian.

Hence, it seems to exist ambiguity on both sides. A complete discussion regarding this topic is out of the scope of this thesis. Yet, it is acknowledged that it might induce some unquantifiable error.

6.1.3 Forward model boundary conditions

Altough promising, an important assumption remains in the present methodology, namely, model errors. Here, they have been assumed to stem only from uncertain bathymetry, whereas boundary conditions and model physics have been assumed perfect. For instance, *SWAN* has been used as a stand-alone model and the effects of currents on waves have been completely neglected.

But most notably, the offshore wave spectral boundary conditions have been specified from highly accurate in situ measurements. At other sites, these would be acquired from larger-scale ocean forecasts, which would likely have more error. Thus, an interesting extension of this work would be the inclusion of bathymetric and wave boundary conditions errors. *Wilson and Berezhnoy*

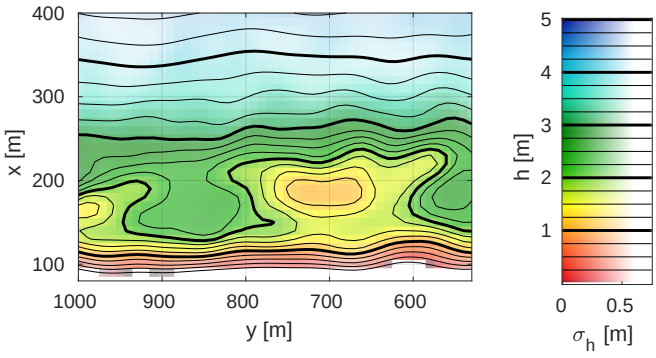

Figure 6.3: Example of the sensitivity to the offshore wave spectral boundary condition (see text).

(2018) have already tackled this problem on an alongshore uniform setup.

To further test this inversion system, it has been applied using a rougher representation of the wave spectrum, as follows. For the whole simulation period, the significant wave height was set at $H_{m0} = 0.85m$, all energy was assumed to be concentrated at the peak period equal to $T_p = 5s$, and directions were assumed to peak at 45° with a 15° standard deviation spread (cf. 5.4). This is obviously a qualitative test, as its results are not objectively compared to the ones presented in section 5.2.2, but from a practical point of view, it is a realistic test, as in general many applications are limited to just bulk wave parameters. As shown in figure 6.3, even with this rough representation of the wave spectrum, the system is able to fairly retrieve the major features of nearshore bathymetry. This result also supports the assumption that model errors are dominated by bathymetry.

6.1.4 Observations uncertainty and bias

As mentioned in section 4.2.3, observational errors were assumed to stem from uncertain wave breaking detection. However, as was shown in section 6.1.1, results depend strongly on the wave-front slope angle, which is an uncertain parameter of the observations. As such, it could have been included in the assimilation method too, but it was decided to leave it aside and resolve a new inversion problem for each θ value for the following reason.

The ensemble Kalman filter was developed to work under the assumption of both unbiased model predictions and observations (*Evensen* (2009)). Yet, such an assumption is hard to evaluate given the lack of other measuring technique capable of producing spatial distributions of roller dissipation as the one developed by *Díaz et al.* (2017). In that context, the roller front slope angle is a major source of observational bias, and its true value is still an open question (*Zhang et al.* (2017)). So, it was decided for the inversion technique to be independent of the roller angle.

However, the methodology followed in this work could open new avenues to study the roller front slope angle distribution. Future applications, after narrowing down detection issues, could use this approach to invert for both the roller angle and bathymetry. Or, in an application where bathymetry is known, this could be a way to investigate how theta varies spatially and temporally.

6.1.5 Ensemble size

To assess the effect of the ensemble size, the system was tested with increasingly larger ensemble sizes and compared against a 500 member reference run. As shown in figure 6.4, even for the smallest ensemble size tested the effect on the final estimate of bathymetry is not excessive. In fact, the estimated bathymetries are not qualitatively different for any of the tested ensembles. Still, it bears mentioning that figure 6.4 does not reflect the stochastic nature of the EnKF, as only one system run was considered for each ensemble size. In other words, this comparison does not consider the eventual variability forced by the randomness of the initial ensemble. However differences should not be significant (cf. figure 15 from *Wilson et al.* (2014)).

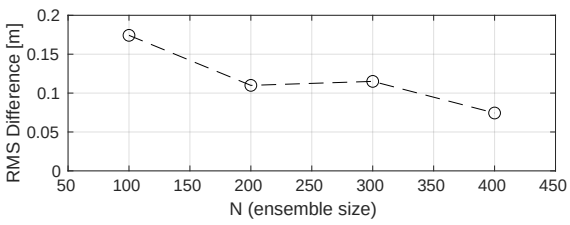

Figure 6.4: Ensemble size assessment. Root-mean-square difference in estimated bathymetry, compared to a reference run with 500 ensemble members. In each case, differences are computed over the domain $100 < x < 300m$.

6.2 Future work

Throughout this thesis, several extensions and improvements have been proposed. These were intimately related to the presented methodology. In this section, the possibilities that arise from this work results are briefly discussed.

To the author's knowledge, this is the first study where physics-based wave breaking dissipation estimates have been used for bathymetry inversion. Results seem promising, especially over nearshore sandbars. However, for a fully reliable bathymetry estimate extensions are needed.

First of all, the wave breaking detection and tracking technique should be further improved. Here, following *Díaz et al.* (2017), a fusion of optical and microwave data was used for this purpose. However, this is not restrictive for the tracking algorithm and the application of *Duncan* (1981) model. In fact, what is needed is a reliable way to capture the roller plan geometry. In that sense, an interesting avenue is to develop a fully optical method. For this purpose, machine learning algorithms have been developed (e.g. *Stringari et al.* (2019)), yet only on cross-shore transects. Extensions of those methods to two-dimension fields would hopefully reduce problems like the one shown in figure 6.2.

On the other hand, as discussed in section 5.2.2, this work methodology is able to reliably estimate bathymetry where wave breaking dissipation is effectively measured (i.e., greater than zero), rather than on a user-specified surf zone domain. Bearing that in mind, a very interesting approach would be to merge the remotely sensed roller dissipation with other wave quantities with an assimilation technique as the one used here. For instance, wave phase velocities from cBathy (*Holman et al.* (2013)) could be used outside the surf zone, and shoreline position estimates on the other side (e.g. *Plant and Holman* (1997)).

Still, for operational applications, a remaining barrier is the need for wave forcing boundary conditions to drive the forward model. To the author's judgment, efforts should be carried to estimate the shallow water wave spectrum from remote sensing data to drive this type of applications. Perhaps, remote estimates of the wave spectrum as the ones proposed by *Holman and Chickadel* (2005) could also be corrected via data assimilation with estimates of wave breaking dissipation.

Chapter 7

Conclusions

The aim of this work was to implement a bathymetry inversion system based on remote sensing estimates of wave breaking dissipation. As a first attempt, physics-based roller dissipation estimates following *Díaz et al.* (2017) were fed into a formal but easy to interpret data assimilation scheme previously shown able to retrieve bathymetry (*Wilson et al.* (2014)).

After a six-hour application, the system was able to retrieve improved bathymetric estimates, without any in situ depth measurement. A prominent feature of this approach is its ability to reliably capture the amplitude and position of a nearshore sandbar, including its interruption by a rip channel. This contrasts with previous approaches based on wave celerity (e.g. *Holman et al.* (2013)), whose accuracy is known to degrade in the surf zone (*Brodie et al.* (2018)), and with applications where optical signals were used as a proxy for dissipation (e.g. *van Dongeren et al.* (2008)).

As mentioned, this approach proved to be effective for surf zone bathymetry inversion. However, future studies might confirm that merging this data product, for instance, with offshore wave celerity estimates should retrieve more complete bathymetric estimates, especially where wave breaking is not the dominant process. Such an extension is feasible in the present approach, where the EnKF can be easily extended for the assimilation of other variables. This suggests applications where the nearshore bathymetry could be continuously monitored only from remote sensing data. Still, a remaining barrier is the need to couple in situ wave data to drive the model-data assimilation comparisons.

Appendix A

Simulation of random fields

Here an outline of *Evensen* (1994a) method for the generation of pseudo-random fields is given. The goal is to simulate N random realizations of bathymetric perturbations $h(x, y)$, which should have zero mean and a given covariance C_{hh}, for the present purposes assumed to be Gaussian.

A smooth field on an $n_x \times n_y$ grid can be written in terms of its Fourier transform as,

$$h(x_n, y_m) = \sum_{l,p} \hat{h}(\kappa_l, \lambda_p) \exp\left(i(\kappa_l x_n + \lambda_p y_m)\right) \Delta k, \tag{A.1}$$

where $x_n = n\Delta x$ and $y_m = m\Delta y$ are the position of the grid points, and

$$\kappa_l = \frac{2\pi l}{n_x \Delta x}, \quad \lambda_p = \frac{2\pi p}{n_y \Delta y}, \quad \Delta k = \frac{(2\pi)^2}{n_x n_y \Delta x \Delta y}, \tag{A.2}$$

are the discrete representation of the wave numbers for each direction.

Further, by taking advantage of the property that the Fourier transform of a Gaussian function is also Gaussian, the Fourier spectrum can be expressed as,

$$\hat{h}(\kappa_l, \lambda_p) = \frac{c}{\sqrt{\Delta k}} \exp\left(-\left(\frac{\kappa_l^2}{r_1^2} + \frac{\lambda_p^2}{r_2^2}\right)\right) \exp\left(2\pi i \phi_{l,p}\right), \tag{A.3}$$

where $\phi_{l,p} \in [0, 1]$ is a uniformly distributed random number used to introduce random phase shifts, r_1 along with r_2 dictate the degree of penalization for high wave numbers and c is an unknown to be determined.

If A.3 is inserted in A.1, the following formula is obtained for the Fourier transform that defines the fields,

$$h(x_n, y_m) = c\sqrt{\Delta k} \sum_{l,p} \exp\left(-\left(\frac{\kappa_l^2}{r_1^2} + \frac{\lambda_p^2}{r_2^2}\right)\right) \exp\left(i(\kappa_l x_n + \lambda_p y_m)\right) \exp\left(2\pi i \phi_{l,p}\right), \tag{A.4}$$

where $\hat{h}(\kappa_l, \lambda_p) = \hat{h}^*(\kappa_{-l}, \lambda_{-p})$, and $Im(\hat{h}(\kappa_0, \lambda_0)) = 0$ have to be imposed to produce real results only.

Taking into consideration the last restrictions, and assuming that fields are uncorrelated in wave space, it can be shown that the covariance between points (x_1, y_1) and (x_2, y_2) is

$$\overline{h(x_1, y_2) h(x_2, y_2)} = \Delta k c^2 \sum_{l,p} \exp\left(-2\left(\frac{\kappa_l^2}{r_1^2} + \frac{\lambda_p^2}{r_2^2}\right)\right) \exp\left(i(\kappa_l(x_1 - x_2) + \lambda_p(y_1 - y_2))\right). \tag{A.5}$$

Equation A.5 is the crux of this method. From this relation three equations are derived as follows. First, by setting $x_1 = x_2$ and $y_1 = y_2$ the desired ensemble variance is imposed,

$$\overline{h(x_1, y_1) h(x_1, y_1)} = 1. \tag{A.6}$$

Then, the user specified correlation lengths L_x and L_y, are used in both directions to force

$$\overline{h(x_1, y_1)h(x_1 + L_x, y_1)} = \exp(-1) \tag{A.7}$$

$$\overline{h(x_1, y_1)h(x_1, y_1 + L_y)} = \exp(-1). \tag{A.8}$$

Thus, from the set A.6, A.7 A.8, the parameters r_1, r_2 and c are obtained, and as a result A.4 is used to compute the random fields via an inverse Fourier transform. Following the recomendation of *Evensen* (1994a) the inverse FFT is computed on a grid 1.2 times bigger than the original to ensure non-periodic fields.

Appendix B

Numerical implementation of the roller model

The numerical implementation used to solve the roller energy evolution is here presented. An implicit scheme is used for integrating 4.20 in the cross-shore direction. This is based on Greg Wilson notes.

First, equation 4.20 is written as,

$$\frac{\partial E_r}{\partial x} = AE_r + B\frac{\partial E_r}{\partial y} + C, \tag{B.1}$$

where

$$A = \frac{-1}{c\cos\alpha}\left(\frac{\partial c\cos\alpha}{\partial x} + \frac{\partial c\sin\alpha}{\partial y} + \frac{g\sin\beta}{c}\right), \tag{B.2}$$

$$B = -\tan\alpha, \tag{B.3}$$

$$C = \frac{1}{2c\cos\alpha}D_{br}. \tag{B.4}$$

Furthermore, α is the mean wave direction and c is calculated as the mean wavelenght over the peak period (all variables extracted from the corresponding *SWAN* run).

Next, each term in B.1 is implicitly discretized as,

$$\left(\frac{\partial E}{\partial x}\right)^{j}_{i+1/2} = \frac{E^j_{i+1} - E^j_i}{\Delta x}, \tag{B.5}$$

$$\left(\frac{\partial E}{\partial y}\right)_{i+1/2} = \frac{1}{2}\left[\left(\frac{\partial E}{\partial y}\right)_i + \left(\frac{\partial E}{\partial y}\right)_{i+1}\right], \tag{B.6}$$

$$\left(\frac{\partial E}{\partial y}\right)_i = \frac{E^{j+1}_i - E^{j-1}_i}{2\Delta y}, \tag{B.7}$$

where $i + 1/2$ is a half grid point shoreward than i, and the subscript r is dropped in the roller energy for simplicity.

Substituting B.5, B.6 and B.7 back in B.1, and rearranging yields,

$$\frac{B^j_i}{4\Delta y}E^{j-1}_{i+1} + \left(\frac{1}{\Delta x} - \frac{A^j_i}{2}\right)E^j_{i+1} - \frac{B^j_i}{4\Delta y}E^{j+1}_{i+1} = - \frac{B^j_i}{4\Delta y}E^{j-1}_i + \left(\frac{1}{\Delta x} + \frac{A^j_i}{2}\right)E^j_i + \frac{B^j_i}{4\Delta y}E^{j+1}_i + C^j_i. \tag{B.8}$$

Importantly note that in the last expression A, B, and C, have to be evaluated at $i+1/2$ too.

B.8 defines a system of J (the number of grid points in the alongshore direction) coupled linear equations, which is witten in matrix form as,

$$\left(\frac{1}{\Delta x}\mathbf{I}-\mathbf{A}\right)\{\mathbf{E}_{i+1}\}=\left(\frac{1}{\Delta x}\mathbf{I}+\mathbf{A}\right)\{\mathbf{E}_i\}+\{\mathbf{C}_i\}, \tag{B.9}$$

where $\mathbf{I}$ is the indentity matrix, and $\{\mathbf{E}_i\}$ and $\{\mathbf{C}_i\}$ are the vector arrangements of E_i^j and C_i^j, and

$$\mathbf{A}=\begin{bmatrix} \frac{A_i^1}{2} & \frac{B_i^1}{4\Delta y} & 0 & \dots & \dots & 0 & \frac{-B_i^1}{4\Delta y} \\ \ddots & \ddots & \ddots & & & & \\ 0 & \frac{-B_i^{j-1}}{4\Delta y} & \frac{A_i^{j-1}}{2} & \frac{B_i^{j-1}}{4\Delta y} & 0 & \dots & 0 \\ 0 & \dots & \frac{-B_i^j}{4\Delta y} & \frac{A_i^j}{2} & \frac{B_i^j}{4\Delta y} & 0 & \dots \\ 0 & \dots & 0 & \frac{-B_i^{j+1}}{4\Delta y} & \frac{A_i^{j+1}}{2} & \frac{B_i^{j+1}}{4\Delta y} & 0 \\ & & & & \ddots & \ddots & \ddots \\ \frac{B_i^J}{4\Delta y} & 0 & \dots & \dots & 0 & \frac{B-_i^J}{4\Delta y} & \frac{A_i^J}{2} \end{bmatrix}.$$

Finally, by setting $E_r=0$ at the offshore boundary, i.e., $\{\mathbf{E}_1\}=0$, B.9 is solved for all wet point until the shoreline.

Appendix C

Influence of the initial estimate (an example)

Results in this appendix are shown to support the thought experiment proposed in section 5.2.2, i.e., the influence of the initial bathymetric estimate.

What is proposed in section 5.2.2 is that if the initial estimate was deeper than true depth, the final estimate would be in agreement with in situ surveys in the regions where breaking dissipation is significantly greater than zero. This is, over the sandbar, given that model predicted dissipation would already have been zero elsewhere.

This is easily appreciated in figure C.2, where it can be seen that differences after data assimilation are heavily reduced where dissipation is strong (cf. figure 5.10(c)). Figure C.4(b) also supports this, as can be seen in the prominent mismatch at the secondary terrace ($x \approx 300m$) and in the overestimated depths in the bar trough ($x \approx 150m$).

For completeness, this appendix shows the same figures as section 5.2.2. Interpretation of the figures that were not explicitly mentioned above follows the same logic as in 5.2.2.

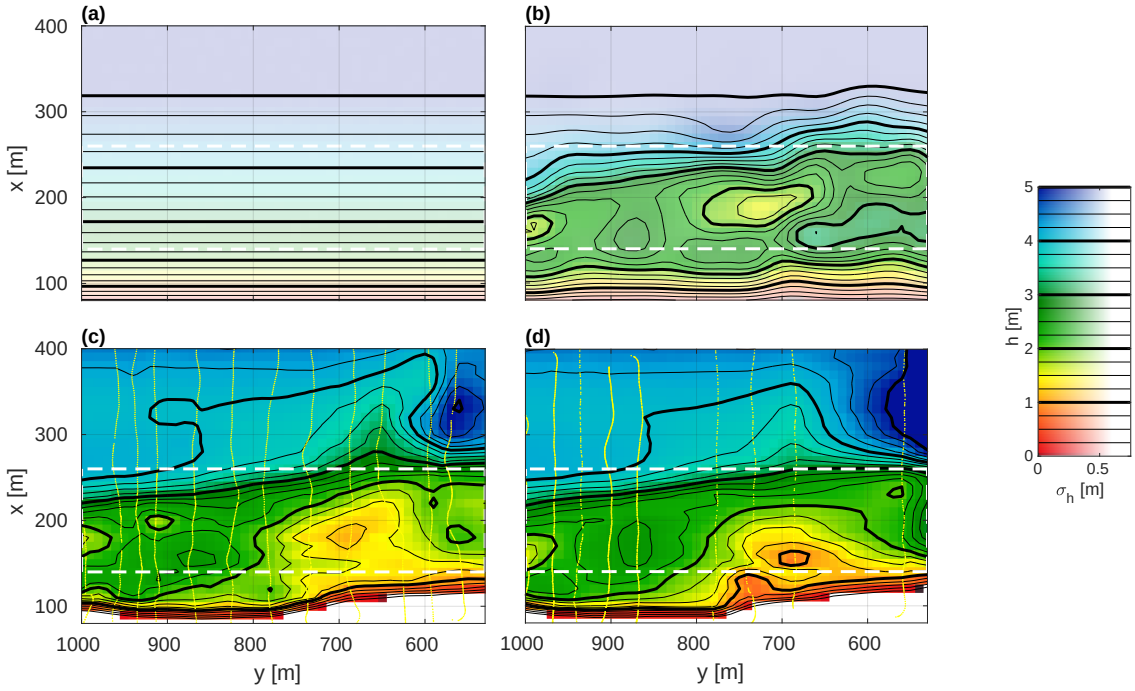

Figure C.1: Results. Initial bathymetry (a), inverted bathymetry after 6 assimilation cycles during 10 Sep. (b), in situ measurements from 6 Sep. (c) and 15 Sep. (d). Yellow dots indicate individual surveyed points and dashed lines are the remote data boundaries. Color bar transparency indicates uncertainty of the estimates. Contour lines apply to all panels. Depths are relative to the NAVD88.

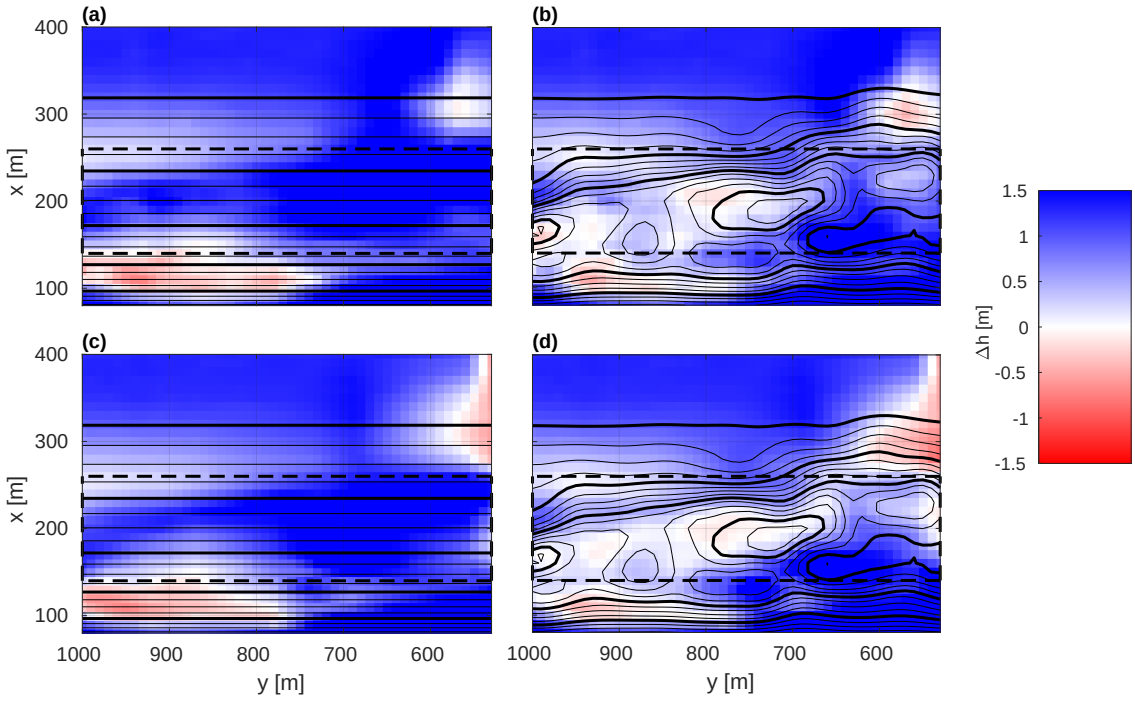

Figure C.2: Difference between estimated bathymetry and gridded survey data. (a) and (b) use data from the 6 Sep., showing differences before and after data assimilation, respectively. (c) and (d) are the same but using data from 15 Sep. Positive differences indicate depth overestimations. Black lines are estimated depth contours as in figure C.1. Dashed lines are remote data boundaries.

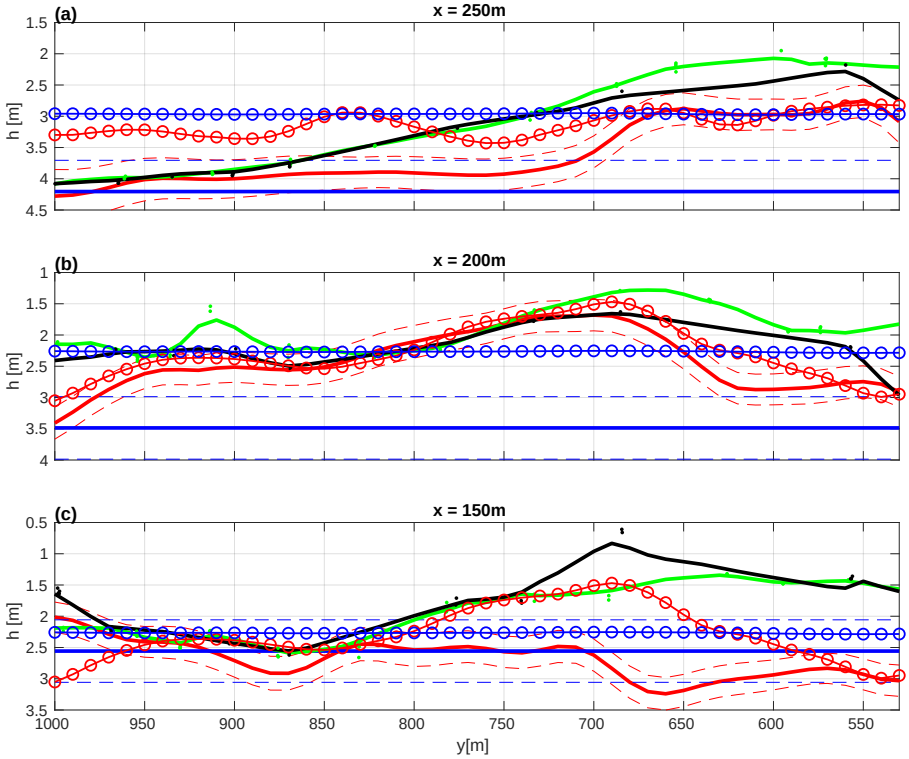

Figure C.3: Alongshore transects at $x = 250m$ (a), $x = 200m$ (b) and $x = 150m$ (c), from initial (thick blue) and final (thick red) estimated bathymetry and $\pm$ one standard deviation (dashed lines), compared to measured bathymetry on 6 Sep. (green) and 15 Sep. (black), and to the initial (dash-dotted in blue) and final (dash-dotted in red) estimates from section 5.2.2. Dots represent measured data from within $2m$ of the alongshore transects; green and black lines are smoothed 2D interpolation of raw data, as in figure C.1.

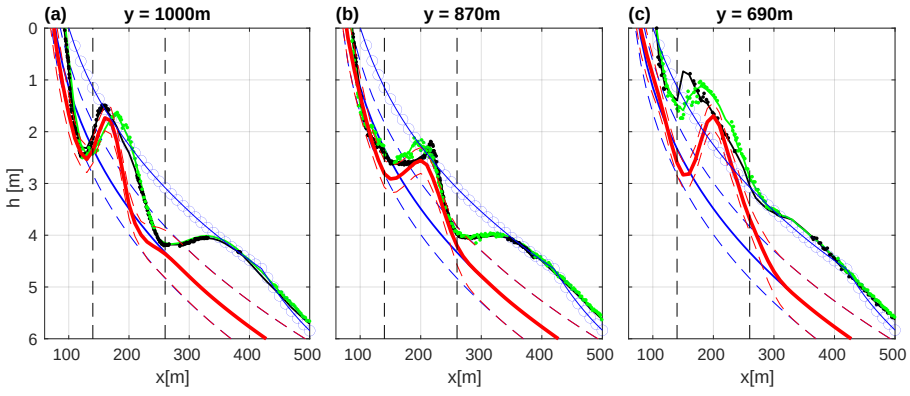

Figure C.4: Cross-shore transects at $y = 1000m$ (a), $y = 870m$ (b) and $y = 690m$ (c), from initial (blue) and final (red) estimated bathymetry and $\pm$ one standard deviation (dashed lines), compared to measured bathymetry on 6 Sep. (green) and 15 Sep. (black), and to the initial estimate from section 5.2.2 (dash-dotted in blue). Dots represent measured data from within $5m$ of the alongshore transects; green and black lines are smoothed 2D interpolation of raw data, as in figure C.1. Vertical dashed lines mark the observed data boundaries.

Appendix D

Additional sensitivity analysis

Figure D.1 shows some sensitivity analyses that were not considered fundamental for section 6.1.1. Yet, they support some statements made in the body of this manuscript. These should be compared to what is shown in figure 5.5.

Results shown in panel (a) were computed with the same parameters as the ones from section 5.2.2, but the initially prescribed bathymetric uncertainty was computed with length scales $L_x = 50m$ and $L_y = 100m$. As appreciated, the initial length scales give similar results, but with slightly less smoothness.

Panel (b) shows the results of a simulation identical to the one from section 5.2.2, but when the roller front slope angle in the forward model is set as $\beta = 24°$. As expected, bathymetry is slightly deeper than what is shown in figure 5.5. Also, in comparison to what is shown in figure 6.1, it can be appreciated that β has a lower influence than θ.

Panel (c) shows the result of an experiment that is set up in with the same parameters as in section 5.2.2, but in this case, the lower bound for the observational errors was defined as 20% of the maximum observed dissipation at each assimilation cycle. Again results are similar. Minor

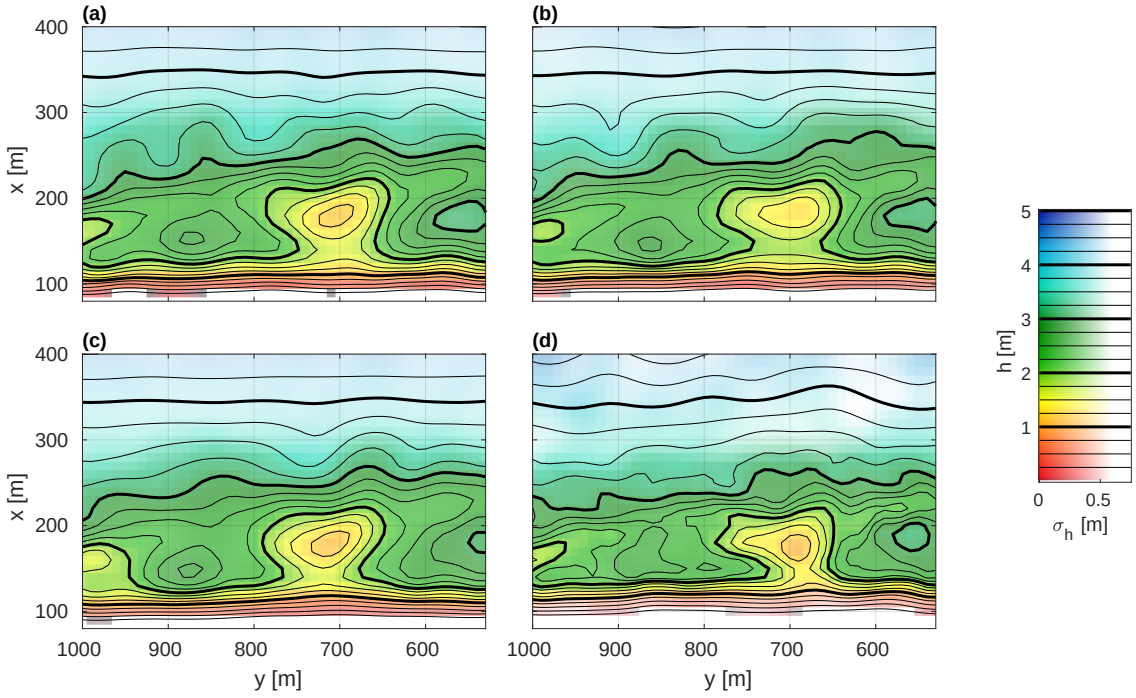

Figure D.1: Additional sensitivity analysis. See text.

changes are due to less belief in the observations where dissipation was zero, i.e., at the observations domain boundary.

Finally, panel (d) is once again a repetition of the experiment from section 5.2.2, but in this case, the localization range for the model error covariance was set as $l_c^f = 37.5m$. Results show spurious sharp contour lines.

Bibliography

Aarninkhof, S., and G. Ruessink (2004), Video observations and model predictions of depth-induced wave dissipation, *Geoscience and Remote Sensing, IEEE Transactions on*, *42*, 2612 – 2622, doi: 10.1109/TGRS.2004.835349.

Aarninkhof, S., G. Ruessink, and D. Roelvink (2005a), Nearshore subtidal bathymetry from time-exposure video images, *Journal of Geophysical Research, 110, 2005 ; doi:10.1029/2004JC002791*, *110*, doi:10.1029/2004JC002791.

Aarninkhof, S., K. Wijnberg, D. Roelvink, and A. Reniers (2005b), *2DH-Quantification of Surf Zone Bathymetry from Video*, pp. 1–14, ,, doi:10.1061/40855(214)64.

Aarninkhof, S. G. J., I. L. Turner, T. D. T. Dronkers, M. Caljouw, and L. Nipius (2003), A video-based technique for mapping intertidal beach bathymetry, *Coastal Engineering*, *49*(4), 275 – 289, doi:https://doi.org/10.1016/S0378-3839(03)00064-4.

Allard, R., J. Dykes, Y. Hsu, J. Kaihatu, and D. Conley (2008), A real-time nearshore wave and current prediction system, *Journal of Marine Systems*, *69*, 37–58, doi:10.1016/j.jmarsys.2007.02.020.

Almar, R., P. Bonneton, N. Senechal, and D. Roelvink (2009), Wave celerity from video imaging: A new method, in *Coastal Engineering 2008*, pp. 661–673, World Scientific Publishing Company, doi:10.1142/9789814277426_0056.

Almar, R., R. Cienfuegos, P. Catalán, F. Birrien, B. Castelle, and H. Michallet (2011), Nearshore bathymetric inversion from video using a fully non-linear boussinesq wave model, *Journal of Coastal Research*, *SI64*, 20–24.

Almar, R., R. Cienfuegos, P. Catalán, H. Michallet, B. Castelle, P. Bonneton, and V. Marieu (2012), A new breaking wave height direct estimator from video imagery, *Coastal Engineering*, *61*, 42–48, doi:10.1016/j.coastaleng.2011.12.004.

Almar, R., E. Bergsma, P. Maisongrande, and L. P. Almeida (2019), Wave-derived coastal bathymetry from satellite video imagery: A showcase with pleiades persistent mode, *Remote Sensing of Environment*, *231*, 111,263, doi:10.1016/j.rse.2019.111263.

Andriolo, U., D. Mendes, and R. Taborda (2020), Breaking wave height estimation from timex images: Two methods for coastal video monitoring systems, *Remote Sensing*, *12*, 204, doi: 10.3390/rs12020204.

Baldock, T. E., P. Holmes, S. Bunker, and P. Van Weert (1998), Cross-shore hydrodynamics within an unsaturated surf zone, *Coastal Engineering*, *34*(3), 173 – 196, doi:https://doi.org/10.1016/S0378-3839(98)00017-9.

Battjes, J., and H. Janssen (1978), Energy loss and set-up due to breaking random waves, *Proceedings of the 16th International Conference on Coastal Engineering*, *1*, doi:10.9753/icce.v16.

Beal, D., P. Brasseur, J.-M. Brankart, Y. Ourmières, and J. Verron (2010), Characterization of mixing errors in a coupled physical biogeochemical model of the north atlantic: implications for nonlinear estimation using gaussian anamorphosis, *Ocean Science*, *6*, 247–262.

Bell, P. S. (1999), Shallow water bathymetry derived from an analysis of x-band marine radar images of waves, *Coastal Engineering*, *37*(3), 513 – 527, doi:https://doi.org/10.1016/S0378-3839(99)00041-1.

Bendat, J., and A. Piersol (2010), *Random Data: Analysis and Measurement Procedures: Fourth Edition*, Wiley Series in Probability ans Statistics, doi:10.1002/9781118032428.

Bennett, A. F. (2002), *Inverse Modeling of the Ocean and Atmosphere*, Cambridge University Press, doi:10.1017/cbo9780511535895.

Bergsma, E., and R. Almar (2018), Video-based depth inversion techniques, a method comparison with synthetic cases, *Coastal Engineering*, *138*, doi:10.1016/j.coastaleng.2018.04.025.

Bergsma, E., D. Conley, M. Davidson, T. O'Hare, and R. Almar (2019), Storm event to seasonal evolution of nearshore bathymetry derived from shore-based video imagery, *Remote Sensing*, *11*, 519, doi:10.3390/rs11050519.

Birkemeier, W. A., and C. Mason (1984), The crab: A unique nearshore surveying vehicle, *Journal of Surveying Engineering*, *110*(1), 1–7, doi:10.1061/(ASCE)0733-9453(1984)110:1(1).

Birrien, F., B. Castelle, V. Marieu, and B. Dubarbier (2013), On a data-model assimilation method to inverse wave-dominated beach bathymetry using heterogeneous video-derived observations, *Ocean Engineering*, *73*, 126–138, doi:10.1016/j.oceaneng.2013.08.002.

Bishop, C. H. (2016), The GIGG-EnKF: ensemble Kalman filtering for highly skewed non-negative uncertainty distributions, *Quarterly Journal of the Royal Meteorological Society*, *142*(696), 1395–1412, doi:10.1002/qj.2742.

Bocquet, M., C. A. Pires, and L. Wu (2010), Beyond Gaussian Statistical Modeling in Geophysical Data Assimilation, *Monthly Weather Review*, *138*(8), 2997–3023, doi:10.1175/2010MWR3164.1.

Booij, N., R. C. Ris, and L. H. Holthuijsen (1999), A third-generation wave model for coastal regions: 1. model description and validation, *Journal of Geophysical Research: Oceans*, *104*(C4), 7649–7666, doi:10.1029/98JC02622.

Bouttier, F., and P. Courtier (1999), *Data Assimilation Concepts and Methods*.

Brodie, K., M. Palmsten, T. Hesser, P. Dickhudt, B. Raubenheimer, H. Ladner, and S. Elgar (2018), Evaluation of video-based linear depth inversion performance and applications using altimeters and hydrographic surveys in a wide range of environmental conditions, *Coastal Engineering*, *136*, doi:10.1016/j.coastaleng.2018.01.003.

Burgers, G., P. Jan van Leeuwen, and G. Evensen (1998), Analysis Scheme in the Ensemble Kalman Filter, *Monthly Weather Review*, *126*(6), 1719–1724, doi:10.1175/1520-0493(1998)126⟨1719:ASITEK⟩2.0.CO;2.

Carini, R., C. Chickadel, A. Jessup, and J. Thomson (2015), Estimating wave energy dissipation in the surf zone using thermal infrared imagery, *Journal of Geophysical Research: Oceans*, *120*, n/a–n/a, doi:10.1002/2014JC010561.

Carrassi, A., M. Bocquet, L. Bertino, and G. Evensen (2018), Data assimilation in the geosciences: An overview of methods, issues, and perspectives, *WIREs Climate Change*, *9*(5), e535, doi:10.1002/wcc.535.

Catalan, P. A. (2008), Microwave scattering from surf zone waves, Phd thesis, Oregon State University.

Catalán, P., and M. Haller (2008), Remote sensing of breaking wave phase speeds with application to nonlinear depth inversion, *Coastal Engineering*, *55*, 93–111, doi:10.1016/j.coastaleng.2007.09.010.

Catalán, P., M. Haller, R. Holman, and W. Plant (2011), Optical and microwave detection of wave breaking in the surf zone, *Geoscience and Remote Sensing, IEEE Transactions on*, *49*, 1879 – 1893, doi:10.1109/TGRS.2010.2095864.

Catalán, P. A., M. C. Haller, and W. J. Plant (2014), Microwave backscattering from surf zone waves, *Journal of Geophysical Research: Oceans*, *119*(5), 3098–3120, doi:10.1002/2014JC009880.

Chickadel, C. C., R. A. Holman, and M. H. Freilich (2003), An optical technique for the measurement of longshore currents, *Journal of Geophysical Research: Oceans*, *108*(C11), doi:10.1029/2003JC001774.

Dally, W., and C. Brown (1995), A modeling investigation of the breaking wave roller with application to cross-shore currents, *Journal of Geophysical Research*, *1002*, 24,873–24,884, doi:10.1029/95JC02868.

Dean, R. G., and R. A. Dalrymple (1991), *Water Wave Mechanics for Engineers and Scientists*, WORLD SCIENTIFIC, doi:10.1142/1232.

Deigaard, R. (1993), A note on the three-dimensional shear stress distribution in a surf zone, *Coastal Engineering*, *20*(1), 157 – 171, doi:https://doi.org/10.1016/0378-3839(93)90059-H.

Dugan, J., W. Morris, K. Vierra, C. Piotrowski, G. Farruggia, and D. Campion (2001a), Jetski-based nearshore bathymetric and current survey system, *Journal of Coastal Research*, *17*, 900–908.

Dugan, J. P., C. C. Piotrowski, and J. Z. Williams (2001b), Water depth and surface current retrievals from airborne optical measurements of surface gravity wave dispersion, *Journal of Geophysical Research: Oceans*, *106*(C8), 16,903–16,915, doi:10.1029/2000JC000369.

Duncan, J. H. (1981), An Experimental Investigation of Breaking Waves Produced by a Towed Hydrofoil, *Proceedings of the Royal Society A: Mathematical, Physical and Engineering Sciences*, *377*(1770), 331–348, doi:10.1098/rspa.1981.0127.

Díaz, H., P. Catalán, and G. Wilson (2017), Quantification of Two-Dimensional Wave Breaking Dissipation in the Surf Zone from Remote Sensing Data, *Remote Sensing*, *10*(2), 38, doi:10.3390/rs10010038.

Evensen, G. (1994a), Sequential data assimilation with a nonlinear quasi-geostrophic model using Monte Carlo methods to forecast error statistics, *Journal of Geophysical Research: Oceans*, *99*(C5), 10,143–10,162, doi:10.1029/94JC00572.

Evensen, G. (1994b), Inverse methods and data assimilation in nonlinear ocean models, *Physica D: Nonlinear Phenomena*, *77*(1), 108 – 129, doi:https://doi.org/10.1016/0167-2789(94)90130-9.

Evensen, G. (2004), Sampling strategies and square root analysis schemes for the EnKF, *Ocean Dynamics*, *54*, 539–560, doi:10.1007/s10236-004-0099-2.

Evensen, G. (2009), *Data Assimilation: The Ensemble Kalman Filter*, Springer-Verlag GmbH.

Flores, R., P. Catalán, and M. Haller (2016), Estimating surfzone wave transformation and wave setup from remote sensing data, *Coastal Engineering*, *114*, doi:10.1016/j.coastaleng.2016.04.008.

Gallagher, E. L., W. Boyd, S. Elgar, R. T. Guza, and B. Woodward (1996), Performance of a sonar altimeter in the nearshore, *Marine Geology*, *133*(3), 241 – 248, doi:https://doi.org/10.1016/0025-3227(96)00018-7.

Gaspari, G., and S. E. Cohn (1999), Construction of correlation functions in two and three dimensions, *Quarterly Journal of the Royal Meteorological Society*, *125*(554), 723–757, doi:10.1002/qj.49712555417.

Ghorbanidehno, H., J. Lee, M. Farthing, T. Hesser, P. K. Kitanidis, and E. F. Darve (2019), Novel Data Assimilation Algorithm for Nearshore Bathymetry, *Journal of Atmospheric and Oceanic Technology*, *36*(4), 699–715, doi:10.1175/JTECH-D-18-0067.1.

Guza, R. T., and E. B. Thornton (1980), Local and shoaled comparisons of sea surface elevations, pressures, and velocities, *Journal of Geophysical Research: Oceans*, *85*(C3), 1524–1530, doi:10.1029/JC085iC03p01524.

Haithuan, D., R. Almar, P. Marchesiello, and N. Viet (2019), Video sensing of nearshore bathymetry evolution with error estimate, *Journal of Marine Science and Engineering*, *7*, 233, doi:10.3390/jmse7070233.

Haller, M., and P. Catalán (2009), Remote sensing of wave roller lengths in the laboratory, *Journal of Geophysical Research: Oceans*, doi:10.1029/2008JC005185.

Haller, M., D. Honegger, and P. Catalán (2014), Rip current observations via marine radar, *Journal of Waterway Port Coastal and Ocean Engineering*, *140*, 115–124, doi:10.1061/(ASCE)WW.1943-5460.0000229.

Hamill, T. M., J. S. Whitaker, and C. Snyder (2001), Distance-Dependent Filtering of Background Error Covariance Estimates in an Ensemble Kalman Filter, *Monthly Weather Review*, *129*(11), 2776–2790, doi:10.1175/1520-0493(2001)129⟨2776:DDFOBE⟩2.0.CO;2.

Holland, T. K. (2001), Application of the linear dispersion relation with respect to depth inversion and remotely sensed imagery, *Geoscience and Remote Sensing, IEEE Transactions on*, *39*, 2060 – 2072, doi:10.1109/36.951097.

Holman, R., and C. Chickadel (2005), Optical remote sensing estimates of the incident wave angle field during ncex, pp. 1072–1081, doi:10.1142/9789812701916_0085.

Holman, R., and M. C. Haller (2013), Remote sensing of the nearshore, *Annual Review of Marine Science*, *5*(1), 95–113, doi:10.1146/annurev-marine-121211-172408, pMID: 22809186.

Holman, R., N. Plant, and T. Holland (2013), cBathy: A robust algorithm for estimating nearshore bathymetry, *Journal of Geophysical Research: Oceans*, *118*(5), 2595–2609, doi:10.1002/jgrc.20199.

Holman, R., K. Brodie, and N. Spore (2017), Surf zone characterization using a small quadcopter: Technical issues and procedures, *IEEE Transactions on Geoscience and Remote Sensing*, *PP*, 1–11, doi:10.1109/TGRS.2016.2635120.

Holman, R. A., and J. Stanley (2007), The history and technical capabilities of argus, *Coastal Engineering*, *54*(6), 477 – 491, doi:https://doi.org/10.1016/j.coastaleng.2007.01.003, the CoastView Project: Developing coastal video monitoring systems in support of coastal zone management.

Holthuijsen, L. (2007), Waves in oceanic and coastal waters, *Waves in Oceanic and Coastal Waters, by Leo H. Holthuijsen, pp. 404. Cambridge University Press, January 2007. ISBN-10: . ISBN-13:*, doi:10.2277/0521860288.

Honegger, D., M. Haller, and R. Holman (2019), High-resolution bathymetry estimates via x-band marine radar: 1. beaches, *Coastal Engineering*, *149*, doi:10.1016/j.coastaleng.2019.03.003.

Honegger, D. A., M. C. Haller, and R. A. Holman (2020), High-resolution bathymetry estimates via x-band marine radar: 2. effects of currents at tidal inlets, *Coastal Engineering*, *156*, 103,626, doi:https://doi.org/10.1016/j.coastaleng.2019.103626.

Horn, R. A., and C. R. Johnson (2012), *Matrix Analysis*, Cambridge University Press.

Houtekamer, P. L., and H. L. Mitchell (2001), A Sequential Ensemble Kalman Filter for Atmospheric Data Assimilation, *Monthly Weather Review*, *129*(1), 123–137, doi:10.1175/1520-0493(2001)129⟨0123:ASEKFF⟩2.0.CO;2.

Inman, D. L., M. H. S. Elwany, and S. A. Jenkins (1993), Shorerise and bar-berm profiles on ocean beaches, *Journal of Geophysical Research: Oceans*, *98*(C10), 18,181–18,199, doi:10.1029/93JC00996.

Irish, J. L., and W. J. Lillycrop (1999), Scanning laser mapping of the coastal zone: the SHOALS system, *ISPRS Journal of Photogrammetry and Remote Sensing*, *54*(2), 123 – 129, doi:https://doi.org/10.1016/S0924-2716(99)00003-9.

Jessup, A., R. A. Holman, C. Chickadel, S. Elgar, G. Farquharson, M. C. Haller, A. L. Kurapov, H. T. Özkan-Haller, B. Raubenheimer, and J. M. Thomson (2012), DARLA: Data Assimilation and Remote Sensing for Littoral Applications, in *AGU Fall Meeting Abstracts*, vol. 2012, pp. OS14A–01.

Kalman, R. E. (1960), A New Approach to Linear Filtering and Prediction Problems, *Journal of Basic Engineering*, *82*(1), 35–45, doi:10.1115/1.3662552.

Kirby, J. T., and T.-M. Chen (1989), Surface waves on vertically sheared flows: Approximate dispersion relations, *Journal of Geophysical Research: Oceans*, *94*(C1), 1013–1027, doi:https://doi.org/10.1029/JC094iC01p01013.

Komar, P. D. (1998), *Beach Processes and Sedimentation*, Prentice Hall.

Kurapov, A. L., and H. T. Özkan-Haller (2013), Bathymetry correction using an adjoint component of a coupled nearshore wave-circulation model: Tests with synthetic velocity data, *Journal of Geophysical Research: Oceans*, *118*(9), 4673–4688, doi:10.1002/jgrc.20306.

Lippmann, T., and R. Holman (1989), Quantification of sand bar morphology: A video technique based on wave dissipation, *J. Geophys. Res.*, *94*, doi:10.1029/JC094iC01p00995.

Lippmann, T., and R. Holman (1990), The spatial and temporal variability of sand bar Morphology, *J. Geophys. Res.*, *95*, doi:10.1029/JC095iC07p11575.

Lippmann, T. C., A. H. Brookins, and E. B. Thornton (1996), Wave energy transformation on natural profiles, *Coastal Engineering*, *27*(1), 1 – 20, doi:https://doi.org/10.1016/0378-3839(95)00036-4.

Long, C. E. (1996), Index and bulk parameters for frequency-direction spectra measured at CERC Field Research Facility, June 1994 to August 1995, doi:10.21236/ada310518, miscellaneous Paper No. CERC-96-6.

Mobley, C. D. (1994), *Light and Water: Radiative Transfer in Natural Waters*, Academic Press.

Moghimi, S., H. T. Özkan Haller, G. W. Wilson, and A. Kurapov (2016), Data Assimilation for Bathymetry Estimation at a Tidal Inlet, *Journal of Atmospheric and Oceanic Technology*, *33*(10), 2145–2163, doi:10.1175/JTECH-D-14-00188.1.

Monfort, C. L., and T. C. Lippmann (2011), Assimilation of Airborne Imagery with a Wave Model for Bathymetric Estimation, *Journal of Coastal Research*, *2011*(10062), 40 – 49, doi:10.2112/SI_62_5.

Piotrowski, C., and J. P. Dugan (2003), Accuracy of bathymetry and current retrievals from airborne optical time-series imaging of shoaling waves, *Geoscience and Remote Sensing, IEEE Transactions on*, *40*, 2606 – 2618, doi:10.1109/TGRS.2002.807578.

Plant, N., T. K. Holland, and M. Haller (2008), Ocean wavenumber estimation from wave-resolving time series imagery, *Geoscience and Remote Sensing, IEEE Transactions on*, *46*, 2644 – 2658, doi:10.1109/TGRS.2008.919821.

Plant, N. G., and R. A. Holman (1997), Intertidal beach profile estimation using video images, *Marine Geology*, *140*(1), 1 – 24, doi:https://doi.org/10.1016/S0025-3227(97)00019-4.

Reniers, A. J. H. M., J. A. Roelvink, and E. B. Thornton (2004), Morphodynamic modeling of an embayed beach under wave group forcing, *Journal of Geophysical Research: Oceans*, *109*(C1), doi:10.1029/2002JC001586.

Ruessink, B. G., J. R. Miles, F. Feddersen, R. T. Guza, and S. Elgar (2001), Modeling the alongshore current on barred beaches, *Journal of Geophysical Research: Oceans*, *106*(C10), 22,451–22,463, doi:10.1029/2000JC000766.

Ruessink, B. G., P. S. Bell, I. M. J. van Enckevort, and S. G. J. Aarninkhof (2002), Nearshore bar crest location quantified from time-averaged x-band radar images, *Coastal Engineering*, *45*(1), 19 – 32, doi:https://doi.org/10.1016/S0378-3839(01)00042-4.

Ruessink, B. G., D. J. R. Walstra, and H. N. Southgate (2003), Calibration and verification of a parametric wave model on barred beaches, *Coastal Engineering*, *48*(3), 139–149.

Rutten, J., S. M. de Jong, and G. Ruessink (2017), Accuracy of nearshore bathymetry inverted from X -band radar and optical video data, *IEEE Transactions on Geoscience and Remote Sensing*, *55*(2), 1106–1116.

Salmon, J. E., L. H. Holthuijsen, M. Zijlema, G. P. van Vledder, and J. D. Pietrzak (2015), Scaling depth-induced wave-breaking in two-dimensional spectral wave models, *Ocean Modelling*, *87*, 30 – 47, doi:https://doi.org/10.1016/j.ocemod.2014.12.011.

Simarro, G., D. Calvete, P. Luque, A. Orfila, and F. Ribas (2019), Ubathy: A new approach for bathymetric inversion from video imagery, *Remote Sensing*, *11*(23), 2722, doi:10.3390/rs11232722.

Simon, E., and L. Bertino (2009), Application of the Gaussian anamorphosis to assimilation in a 3-D coupled physical-ecosystem model of the North Atlantic with the EnKF: a twin experiment., *Ocean Science*, *5*(4).

Stive, M. J. F., and H. J. De Vriend (1994), Shear stresses and mean flow in shoaling and breaking waves, *Coastal Engineering Proceedings*, *1*(24), doi:10.9753/icce.v24.%p.

Stockdon, H. F., and R. A. Holman (2000), Estimation of wave phase speed and nearshore bathymetry from video imagery, *Journal of Geophysical Research: Oceans*, *105*(C9), 22,015–22,033, doi:10.1029/1999JC000124.

Stringari, C., D. Harris, and H. Power (2019), A novel machine learning algorithm for tracking remotely sensed waves in the surf zone, *Coastal Engineering*, *147*, doi:10.1016/j.coastaleng.2019.02.002.

Stringari, C. E., and H. E. Power (2019), The fraction of broken waves in natural surf zones, *Journal of Geophysical Research: Oceans*, *124*(12), 9114–9140, doi:10.1029/2019JC015213.

Svendsen, I. A. (1984), Wave heights and set-up in a surf zone, *Coastal Engineering*, *8*(4), 303 – 329, doi:https://doi.org/10.1016/0378-3839(84)90028-0.

Thornton, E., and R. Guza (1983), Transformation of wave height distribution, *Journal of Geophysical Research*, *88*, 5925–5938, doi:10.1029/JC088iC10p05925.

Thornton, E. B., and R. T. Guza (1982), Energy saturation and phase speeds measured on a natural beach, *Journal of Geophysical Research: Oceans*, *87*(C12), 9499–9508, doi:10.1029/JC087iC12p09499.

van der Westhuysen, A. J. (2010), Modeling of depth-induced wave breaking under finite depth wave growth conditions, *Journal of Geophysical Research: Oceans*, *115*(C1), doi:10.1029/2009JC005433.

van Dongeren, A., N. Plant, A. Cohen, D. Roelvink, M. C. Haller, and P. Catalán (2008), Beach wizard: Nearshore bathymetry estimation through assimilation of model computations and remote observations, *Coastal Engineering*, *55*(12), 1016 – 1027, doi:https://doi.org/10.1016/j.coastaleng.2008.04.011.

van Enckevort, I. M. J., B. G. Ruessink, G. Coco, K. Suzuki, I. L. Turner, N. G. Plant, and R. A. Holman (2004), Observations of nearshore crescentic sandbars, *Journal of Geophysical Research: Oceans*, *109*(C6), doi:10.1029/2003JC002214.

van Leeuwen, P. J., and G. Evensen (1996), Data Assimilation and Inverse Methods in Terms of a Probabilistic Formulation, *Monthly Weather Review*, *124*(12), 2898–2913, doi:10.1175/1520-0493(1996)124⟨2898:DAAIMI⟩2.0.CO;2.

Williams, W. W. (1947), The determination of gradients on enemy-held beaches, *The Geographical Journal*, *109*(1/3), 76–90.

Wilson, G., and S. Berezhnoy (2018), Surfzone State Estimation, with Applications to Quadcopter-Based Remote Sensing Data, *Journal of Atmospheric and Oceanic Technology*, *35*(10), 1881–1896, doi:10.1175/JTECH-D-17-0205.1.

Wilson, G. W., H. T. Özkan Haller, and R. A. Holman (2010), Data assimilation and bathymetric inversion in a two-dimensional horizontal surf zone model, *Journal of Geophysical Research: Oceans*, *115*(C12), doi:10.1029/2010JC006286.

Wilson, G. W., H. T. Özkan Haller, R. A. Holman, M. C. Haller, D. A. Honegger, and C. C. Chickadel (2014), Surf zone bathymetry and circulation predictions via data assimilation of remote sensing observations, *Journal of Geophysical Research: Oceans*, *119*(3), 1993–2016, doi:10.1002/2013JC009213.

Zhang, C., Q. Zhang, J. Zheng, and Z. Demirbilek (2017), Parameterization of nearshore wave front slope, *Coastal Engineering*, *127*, 80 – 87, doi:https://doi.org/10.1016/j.coastaleng.2017.06.008.